

Supplemental Information

Side Chain Engineering Control of Mixed Conduction in Oligoethylene Glycol-Substituted Polythiophenes

*Jonathan W. Onorato,^{A, †} Zhongyang Wang,^{B, †} Yangyang Sun,^C Christian Nowak,^C Lucas Q. Flagg,^D
Ruipeng Li,^E Ban Xuan Dong,^B Lee J. Richter,^D Fernando Escobedo,^C Paul Nealey,^B Shrayesh Patel,^B
Christine K. Luscombe^{A, F, G*}.*

^A ~ Department of Materials Science and Engineering, University of Washington, Seattle, WA 98195, United States.

^B ~ Pritzker School of Molecular Engineering, University of Chicago, Chicago, IL, United States.

^C ~ School of Chemical and Biomolecular Engineering, Cornell University, Ithaca, NY, United States.

^D ~ Materials Science and Engineering Division, National Institute of Standards and Technology, Gaithersburg, Maryland 20899, United States

^E ~ National Synchrotron Light Source II, Brookhaven National Laboratory, Upton, New York, 11973, USA

^F ~ Department of Molecular Engineering, University of Washington, Seattle, WA 98195, United States.

^G Department of Chemistry, University of Washington, Seattle, WA 98195, United States.

† These two authors contributed equally to the work.

* Corresponding Author. E-mail luscombe@uw.edu

Table of Contents

S.1.	Synthesis and Polymer Characterization.....	S3
S.1.1	Monomer Synthesis and Characterization.....	S3
S.1.1.1	Materials and Procedures	S3
S.1.1.2	Synthesis of 2,5-dibromo-3-(7'-methoxyheptyl)thiophene (P3AAPT)	S3
S.1.1.3	Synthesis of 2,5-dibromo-3-(4'-(methoxyethoxy)butyl)thiophene (P3APPT)	S5
S.1.1.4	Synthesis of 2,5-dibromo-3-thiophene methyl bromide	S7
S.1.1.5	Synthesis of 2,5-dibromo-3-(1'-heptoxymethyl)thiophene (P3PAAT)	S8
S.1.1.6	Synthesis of 2,5-dibromo-3-(butoxyethoxymethyl)thiophene (P3PPAT).....	S9
S.1.2	Polymer Synthesis and Characterization.....	S10
S.1.2.1	General Procedure for Polymer Synthesis	S10
S.1.2.2	P3AAPT Synthesis.....	S11
S.1.2.3	P3APPT Synthesis	S11
S.1.2.4	P3PAAT Synthesis.....	S11
S.1.2.5	P3PPAT Synthesis	S12
S.2.	Thermal Analysis of Polymers and Polymer:LiTFSI Blends.....	S13
S.3.	UV-Vis Analysis.....	S16
S.4.	GIWAXS Supplemental Data	S17
S.5.	Atomic Force Microscopy	S24
S.6.	Molecular Dynamics.....	S26
S.6.1	Force Field Parameters	S26
S.6.1.1	Image File: "Chemical-map.png"	S27
S.6.1.2	Text File: "atom-info.txt"	S28
S.6.1.3	Text File: "forcefield-lammps.txt".....	S30
S.6.2	Structure Generation.....	S30
S.6.2.1	Crystalline Morphology.....	S30
S.6.2.2	Amorphous Morphology	S34
S.6.3	Lithium Ion Mobility Calculations	S35
S.6.4	Dissociation Energy and Potential of Mean Force.....	S37
S.6.5	Solvation Shells and Solvation Environments	S39
S.7.	DC measurements for P3AAPT.....	S44
S.8.	SI References.....	S44

S.1. Synthesis and Polymer Characterization
S.1.1 Monomer Synthesis and Characterization
S.1.1.1 Materials and Procedures

3-thiophenemethanol was purchased from TCIⁱ. N-bromosuccinimide, NBS, was purchased from Sigma-Aldrich and recrystallized using a ratio of 100 mL of H₂O to 10 g of NBS. Tetrahydrofuran, THF, was dried and deoxygenated using a PureSolv solvent purification system. Dichloromethane, DCM, was dried and deoxygenated on a SP-1 Stand Alone Solvent Purification System solvent purification system. All other chemicals were purchased from Sigma-Aldrich and used as received. All reactions are performed under air-free conditions, with glassware that was dried overnight in a 120 °C air oven. Material handling notes: Both NaH and PBr₃ have significant hazards that include potentially explosive conditions. Make sure to read the safety data sheets and understand the use cases clearly and carefully to ensure no accidental cross-contamination occurs, and that you remain safe through the reactions.

¹H NMR spectra were recorded on a Bruker AV-300 for all small molecule characterizations, and a Bruker AV-500 for polymer samples, all at 298 K using CDCl₃ as a solvent.

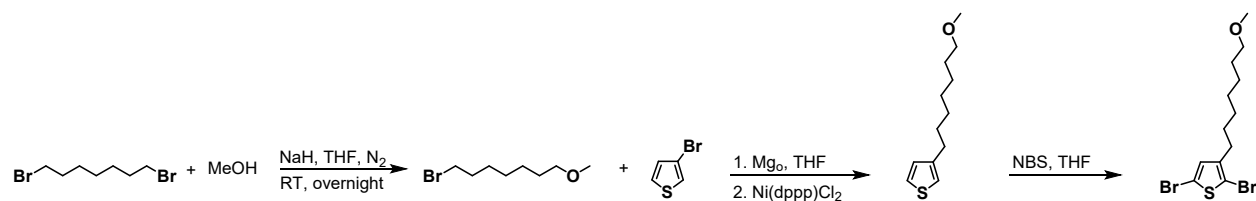


Figure S1: Full synthesis scheme of 2,5-dibromo-3-(7'-methoxyheptyl)thiophene.

S.1.1.2 Synthesis of 2,5-dibromo-3-(7'-methoxyheptyl)thiophene (P3AAPT)
S.1.1.2.1 Synthesis of 7-bromoheptyl methyl ether

1,7-dibromoheptane (6.84 mL, 40 mmol) was added to a round bottom flask, then degassed under high vacuum for approximately 5 min. To a separate flask, anhydrous methanol, MeOH, (0.54 mL,

13.3 mmol) and anhydrous THF (40 mL) were added. NaH (60% dispersion in mineral oil, 0.68 g, 17 mmol) was added in one portion, and the flask was quickly recapped. The NaH was allowed to react over 1 h, then the contents were transferred dropwise to the flask containing the 1,7-dibromoheptane. The reaction was then allowed to stir overnight. The reaction mixture was filtered through a fine frit to remove salt from the mixture. The product was washed through the frit with additional THF, then concentrated using rotary evaporation. The product was purified through silica column chromatography, using an eluent of hexanes/ethyl acetate at a ratio of 90/10, yielding 1.103 g of a clear viscous oil in 40.6 % yield. ¹H NMR (300MHz, CDCl₃ δ): 3.34 (t, 2 H), 3.30 (t, 2H, overlapping with previous), 3.26 (s, 3H), 1.79 (p, 2H), 1.50 (m, 2H), 1.37 (m, 2H), 1.28 (m, 4H).

S.1.1.2.2 Synthesis of 3-(7'-methoxyheptyl)thiophene

Magnesium turnings (1.02 g, 42.4 mmol) were added to a 3-neck flask, and a condenser was added. The magnesium was flame-activated under high vacuum (additional entrainment agents could be used as well to improve yields). Following activation, THF (80 mL) and then 7-bromoheptyl methyl ether (8.390 g, 40.4 mmol) was added to the flask, then refluxed for 2 h. In a separate flask, 3-bromothiophene (3.212 mL, 34.30 mmol), and Ni(dppp)Cl₂ (437.3 mg, 0.807 mmol) were mixed under nitrogen with a small amount of THF (30 mL). The magnesium mixture was cooled to room temperature, and then the nickel mixture was added dropwise to the 7-magnesioheptyl methyl ether over a period of 15 min. After full addition of the 7-magnesioheptyl methyl ether, the reaction was heated to reflux and left to reflux overnight. The reaction was quenched with 150 mL 0.33 M HCl, then extracted 3 times with diethyl ether. The ether was dried over Na₂SO₄, and then concentrated under rotary evaporation. The crude product was purified using silica column chromatography using hexanes as an eluent, resulting in 5.96 g of a pale yellow oil as a product in an 82.0 % yield.

^1H NMR (300MHz, CDCl_3 δ): 7.25 (q, 1H), 6.96 (d, 1H), 6.94 (d, 1H, significant overlap with previous peak), 3.29 (t, 2H), 3.25 (s, 3H), 2.54 (t, 2H), 1.51 (m, 4H), 1.27 (m, 6H).

S.1.1.2.3 Synthesis of 2,5-dibromo-3-(7'-methoxyheptyl)thiophene

To a round bottom flask, 3-(7'-methoxyheptyl)thiophene (5.95 g, 28.1 mmol) and anhydrous THF (26 mL) were added, and nitrogen was bubbled through for 15 min. Following bubbling, NBS (9.942 g, 55.9 mmol) was added in 5 equal portions, capping the reaction in-between each addition. The reaction was stirred overnight covered in foil at room temperature. The reaction was rotovapped to remove all THF, then the solids were filtered over a frit. The product was washed through the frit using hexanes. The hexanes was removed through rotary evaporation, then the crude product was purified using silica column chromatography with hexanes/ethyl acetate in a 95/5 ratio as an eluent, resulting in 5.441 g of a pale yellow oil as a product in a 52.4 % yield. ^1H NMR (300MHz, CDCl_3 δ): 6.78 (s, 1H), 3.37 (t, 2H), 3.34 (s, 3H), 2.51 (t, 2H), 1.57 (m, 4H), 1.35 (m, 6H).

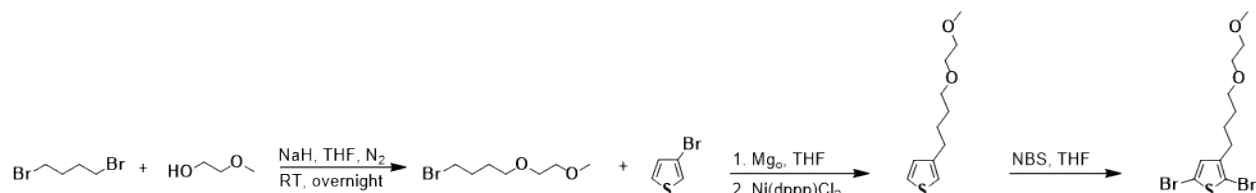


Figure S2: Full synthetic scheme for 2,5-dibromo-3-(4'-(methoxyethoxy)butyl)thiophene.

S.1.1.3 Synthesis of 2,5-dibromo-3-(4'-(methoxyethoxy)butyl)thiophene (P3APPT)

S.1.1.3.1 Synthesis of 4-bromobutyl 2-methoxyethyl ether

1,4-dibromobutane (29.85 mL, 250 mmol) was added to a round bottom flask, then degassed under high vacuum for approximately 5 min. Then, 125 mL of THF was added to the 1,4-dibromobutane. To a separate flask, anhydrous 2-methoxyethanol (3.94 mL, 50 mmol) and anhydrous THF (75 mL) were added. NaH (60% dispersion in mineral oil, 2.5 g, 62.5 mmol) was added in one portion,

and the flask was quickly recapped. The NaH was allowed to react over 10 min, then the contents were transferred dropwise to the flask containing the 1,4-dibromobutane. The reaction was then allowed to stir overnight. The reaction mixture was filtered through a fine frit to remove salt from the mixture. The product was washed through the frit with additional THF, then concentrated under rotary evaporation. The product was purified through silica column chromatography, using an eluent of hexanes/ethyl acetate at a ratio of 60/40, yielding 10.650 g of a clear viscous oil in 32.7 % yield. ¹H NMR (300MHz, CDCl₃ δ): 3.47 (m, 4H), 3.43 (t, 2H), 3.36 (t, 2H), 3.29 (s, 3H), 1.87 (m, 2H), 1.66 (m, 2H).

S.1.1.3.2 Synthesis of 3-(4'-(methoxyethoxy)butyl)thiophene

Magnesium turnings (1.97 g, 82.2 mmol) were added to a 3-neck flask, and a condenser was added. The magnesium was flame-activated under high vacuum (additional entrainment agents could be used as well to improve yields). Following activation, THF (80 mL) and then 4-bromobutyl 2-methoxyethyl ether (16.684 g, 78.33 mmol) was added to the flask, then refluxed for 2 h. In a separate flask, 3-bromothiophene (6.24 mL, 66.58 mmol), and Ni(dppp)Cl₂ (850 mg, 1.57 mmol) were mixed under nitrogen with a small amount of THF (40 mL). The magnesium mixture was cooled to room temperature, and then the nickel mixture was added dropwise to the 4-magnesiobutyl-2'-methoxyethyl ether over a period of 15 min. After full addition of the 4-magnesiobutyl 2-methoxyethyl ether, the reaction was heated, and refluxed overnight. The reaction was quenched with 150 mL 0.33 M HCl, then extracted 3 times with diethyl ether. The ether was dried over Na₂SO₄, and then concentrated under rotary evaporation. The crude product was purified using silica column chromatography using hexanes/ethyl acetate at a 70/30 ratio as an eluent, resulting in 7.468 g of a pale yellow oil as a product in a 51.5 % yield. ¹H NMR

(300MHz, CDCl₃ δ): 7.19 (q, 1H), 6.91 (d, 1H), 3.53 (m, 4H), 3.46 (t, 2H), 3.36 (s, 3H), 2.63 (t, 2H), 1.66 (m, 4H)

S.1.1.3.3 Synthesis of 2,5-dibromo-3-(4'-(methoxyethoxy)butyl)thiophene

To a round bottom flask, 3-(4'-(methoxyethoxy)butyl)thiophene (7.468 g, 35.4 mmol) and anhydrous THF (32.2 mL) were added, and nitrogen was bubbled through for 15 min. Following bubbling, NBS (12.58 g, 70.4 mmol) was added in 5 equal portions, capping the reaction in-between each addition. The reaction was stirred overnight covered in foil at room temperature. The reaction was rotovapped to remove all THF, then the solids were filtered over a frit. The product was washed through the frit using hexanes. The hexanes was removed through rotary evaporation, then the crude product was purified using silica column chromatography with hexanes/ethyl acetate in a 90/10 ratio as an eluent, resulting in 10.2314 g of a pale yellow oil as a product in a 78.5 % yield. ¹H NMR (300MHz, CDCl₃ δ): 6.98 (s, 1H), 3.74 (m, 4H), 3.66 (t, 2H), 3.57 (s, 3H), 2.73 (t, 2H), 1.82 (m, 4H).

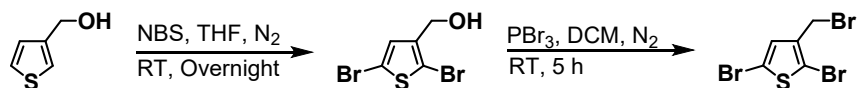


Figure S3: Synthetic scheme for the synthesis of 2,5-dibromo-3-thiophene methyl bromide.

The next two monomer syntheses start from this core synthesis (Figure S3). This synthesis has been described previously but will be reported herein for clarity and completeness.^{1,2}

S.1.1.4 Synthesis of 2,5-dibromo-3-thiophene methyl bromide

S.1.1.4.1 Synthesis of 2,5-dibromo-3-thiophenemethanol

To a 3-neck flask, 3-thiophenemethanol (4.13 mL, 43.8 mmol) and anhydrous THF (40 mL) are added. The solution is degassed by bubbling nitrogen for 15 min, then NBS (15.5 g, 87 mmol) is added in 5 equal portions, allowing time to stir in between additions. The mixture is then stirred overnight at room temperature. After reacting, the solvent is removed by rotary evaporation. The

residue is washed with hexanes and filtered, rinsing until the rinsate is no longer UV-active upon spotting on silica plate. The product was purified by eluting over silica gel with a 4:1 mixture of hexanes to ethyl acetate. The product was collected as 10.745 g of a white solid in 90.9 % yield. ^1H NMR (300MHz, CDCl_3 δ): 7.03 (s, 1H), 4.57 (s, 2H), 1.96 (s, broad and variable, 1H).

S.1.1.4.2 Synthesis of 2,5-dibromo-3-thiophenemethylbromide

To a round bottom flask, 2,5-dibromo-3-thiophenemethanol (4.204 g, 15.6 mmol) and anhydrous DCM (80 mL) were added. The flask was placed on ice for 20 min, then PBr_3 (1.50 mL, 15.9 mmol) was added dropwise over 15 min. The reaction was allowed to stir at room temperature for 5 h. The reaction was quenched by addition of a 10% aqueous NaHCO_3 solution. The product was extracted with dichloromethane, washed with brine, then dried with MgSO_4 and filtered. The solvent was removed, and the product was stored at -20 °C overnight, after which a white solid was collected in 92.5 % yield. ^1H NMR (300MHz, CDCl_3 δ): 7.00 (s, 1H), 4.37 (s, 2H).

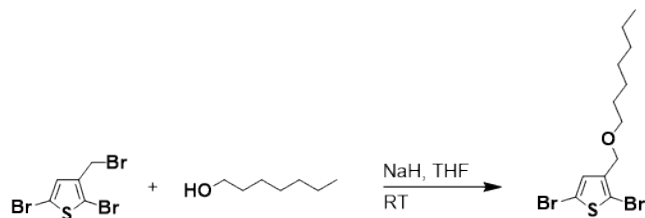


Figure S4: Synthetic scheme of 2,5-dibromo-3-(1'-heptoxymethyl)thiophene.

S.1.1.5 Synthesis of 2,5-dibromo-3-(1'-heptoxymethyl)thiophene (P3PAAT)

S.1.1.5.1 Synthesis of 2,5-dibromo-3-(1'-heptoxymethyl)thiophene

Anhydrous 1-heptanol (6.285 mL, 44.5 mmol) and THF (120 mL) were added to a 3-neck flask with an attached addition funnel. Then, NaH (60% dispersion in mineral oil, 2.027 g, 50.7 mmol) was quickly added in one portion, and the NaH was allowed to react for 2 h (note that this time is significantly longer than is needed for the synthesis of 2,5-dibromo-3-(methoxyethoxyethoxymethyl)thiophene; it appears that the 1-heptanol reacts at a significantly

slower rate than diethylene glycol monomethyl ether). 2,5-dibromo-3-thiophenemethylbromide (14.270 g, 40.4 mmol) was dissolved in THF (60 mL), then added to the addition funnel. The 2,5-dibromo-3-thiophenemethylbromide was added dropwise over a period of 15 min, then stirred at room temperature overnight. The reaction mixture was filtered over a thin pad of Celite, then the product was washed through with THF. The solvent was removed using rotary evaporation, and the product was purified through column chromatography in pure hexanes. Note that initial thin-layer chromatography shows un-representative values due to the influence of residual 1-heptanol on the R_f of the product. The product was collected as 13.777 g in an 91.6 % yield as a pale yellow oil, and was stored at -20 °C. ^1H NMR (300MHz, CDCl_3 δ): 6.96 (s, 1H), 4.35 (s, 2H), 3.43 (t, 2H), 1.60 (p, 2H), 1.30 (m, 6H), 0.89 (t, 3H).

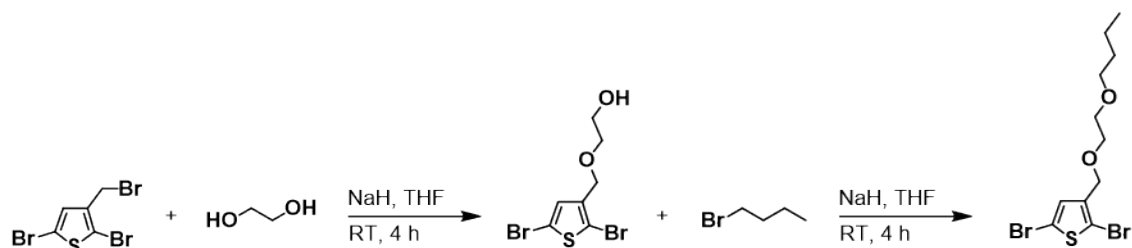


Figure S5: Synthetic scheme of 2,5-dibromo-3-(butoxyethoxymethyl)thiophene.

S.1.1.6 Synthesis of 2,5-dibromo-3-(butoxyethoxymethyl)thiophene (P3PPAT)

S.1.1.6.1 Synthesis of 2,5-dibromo-3-(2-hydroxyethoxymethyl)thiophene

Ethylene glycol (9.53 mL, 170.1 mmol) and THF (20 mL) were added to a 3-neck flask with an attached addition funnel. Then, NaH (60% dispersion in mineral oil, 1.432 g, 35.81 mmol) was quickly added in one portion, and the NaH was allowed to react for 2 h. 2,5-dibromo-3-thiophenemethylbromide (9.21 g, 34.1 mmol) was dissolved in THF (15 mL), then added to the addition funnel. The 2,5-dibromo-3-thiophenemethylbromide was added dropwise over a period of 15 min, then stirred at room temperature overnight. The reaction mixture was filtered over a thin pad of Celite, then the product was washed through with THF. The solvent was removed using

rotary evaporation, and the product was purified through column chromatography in hexanes/ethyl acetate at a 70/30 ratio. The product was collected as 7.140 g in an 83.1 % yield as a pale-yellow solid. ¹H NMR (300MHz, CDCl₃ δ): 6.94 (s, 1H), 4.38 (s, 2H), 3.67 (t, 2H), 3.51 (t, 2H), 3.06 (s, broad and variable, 1H).

S.1.1.6.2 Synthesis of 2,5-dibromo-3-(butoxyethoxymethyl)thiophene

Anhydrous 1-bromobutane (9.295 mL, 85 mmol) and THF (80 mL) were added to a 3-neck flask with an attached addition funnel. Then, NaH (60% dispersion in mineral oil, 1.19 g, 29.7 mmol) was quickly added in one portion, and the NaH was allowed to react for 30 min. 2,5-dibromo-3-(2-hydroxyethoxymethyl)thiophene (7.14 g, 28.33 mmol) was dissolved in THF (40 mL), then added to the addition funnel. The 2,5-dibromo-3-(2-hydroxyethoxymethyl)thiophene was added dropwise over a period of 15 min, then stirred at room temperature overnight. The reaction mixture was filtered over a thin pad of Celite, then the product was washed through with THF. The solvent was removed using rotary evaporation, and the product was purified through column chromatography in hexanes/ethyl acetate at a 95/5 ratio. The product was collected as 1.131 g in a 10.7 % yield as a pale yellow oil, and stored at -20 °C. ¹H NMR (300MHz, CDCl₃ δ): 6.99 (s, 1H), 4.43 (s, 2H), 3.58 (m, 4H), 3.44 (t, 2H), 1.58 (p, 2H), 1.37 (p, 2H), 0.91 (t, 3H).

S.1.2 Polymer Synthesis and Characterization

S.1.2.1 General Procedure for Polymer Synthesis

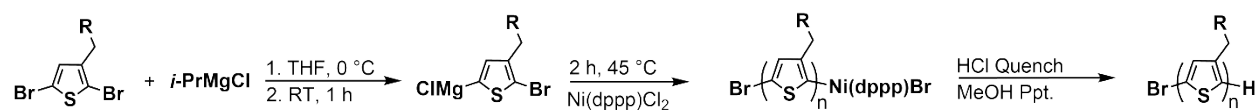


Figure S6: Generalized synthetic scheme showing the 1-pot synthesis of the conjugated polymers from their respective dibrominated monomers.

A generalized procedure for the polymerization of all monomers is shown in Figure S6. All polymers made herein follow this procedure. To a dried Schlenk flask, dibrominated monomer (5 mmol) was added, and then degassed under high vacuum for 30 min. Following degassing, the flask was returned to a nitrogen atmosphere, and the monomer was diluted with 50 mL of anhydrous THF. The monomer was stirred rapidly, and then was cooled to 0 °C, and *i*-PrMgCl (2.475 mL, 4.95 mmol, 2.0 M) was added dropwise over 10 min. The flask was then warmed to room temperature and allowed to stir for 1 h. When the Grignardization is complete, the flask is placed in an oil bath at 45 °C. Then, Ni(dppp)Cl₂ (23.331 mg, 0.0430 mmol) is added quickly and in one portion with rapid stirring, and the flask is quickly recapped. The polymerization was allowed to continue for 2 h, and then was quenched with 5 mL of 5M HCl, then precipitated into MeOH. The polymer was collected by filtration. The solid polymer powder was purified by Soxhlet extraction, using first MeOH, and then the purified polymer was extracted with CHCl₃. The purified polymer was again precipitated into MeOH and collected by filtration.

S.1.2.2 P3AAPT Synthesis

Following the above general procedure, 272.3 mg of P3AAPT was synthesized with $M_n = 12.4$ kg/mol, polydispersity, $D = 1.38$. ¹H NMR (500MHz, CDCl₃ δ): 6.98 (s, 1H), 3.36 (t, 2H), 3.32 (s, 3H), 2.80 (t, 2H), 1.71 (m, 2H), 1.57 (m, 4H), 1.43 (m, 2H), 1.38 (m, 4H).

S.1.2.3 P3APPT Synthesis

Following the above general procedure, 250.5 mg of P3APPT was synthesized with $M_n = 10.5$ kg/mol, $D = 1.51$. ¹H NMR (500MHz, CDCl₃ δ): 6.99 (s, 1H), 3.59 (m, 2H), 3.54 (m, 4H), 3.38 (s, 3H), 2.84 (t, 2H), 1.76, (m, 4H).

S.1.2.4 P3PAAT Synthesis

Following the above general procedure, 258.9 mg of P3PAAT was synthesized with $M_n = 9.1$ kg/mol, $D = 1.91$. $^1\text{H NMR}$ (500MHz, CDCl_3 δ): 7.24 (s, 1H), 4.58 (d, 2H with 4.42), 4.42 (d, 2H with 4.58), 3.56 (d, 2H with 3.45), 3.45 (d, 2H with 3.56), 1.56 (m, 4H), 1.29 (m, 6H), 0.87 (t, 3H).

S.1.2.5 P3PPAT Synthesis

Following the above general procedure, 130.0 mg of P3PPAT was synthesized with $M_n = 12.4$ kg/mol, $D = 1.49$. $^1\text{H NMR}$ (500MHz, CDCl_3 δ): 7.26 (s, 1H), 4.67 (s, 2H with 4.50), 4.50 (d, 2H with 4.67), 3.71 (t, 2H with 3.60), 3.65 (t, 2H with 3.60), 3.60 (m, 2H with 3.65 and 3.71), 3.49 (m, 2H), 1.58 (m, 2H), 1.37 (m, 2H), 0.90 (t, 3H).

S.2. Thermal Analysis of Polymers and Polymer:LiTFSI Blends

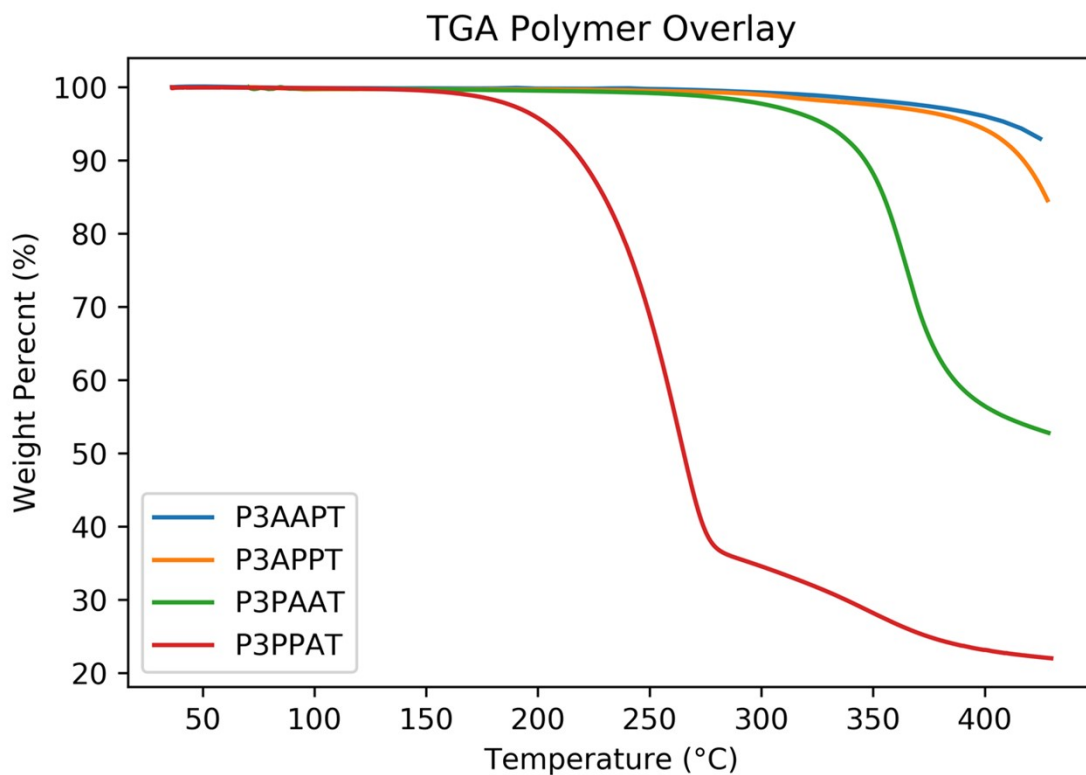


Figure S7: Thermogravimetric analysis, TGA, of neat polymers, showing the onset of thermal degradation.

Thermogravimetric analysis (TGA) data shows that all polymers are thermally stable within the window utilized for electrochemical impedance spectroscopy (EIS). All the polymers have reasonably high degradation temperatures, except P3PPAT which shows a remarkably low thermal degradation onset of around 170 °C.

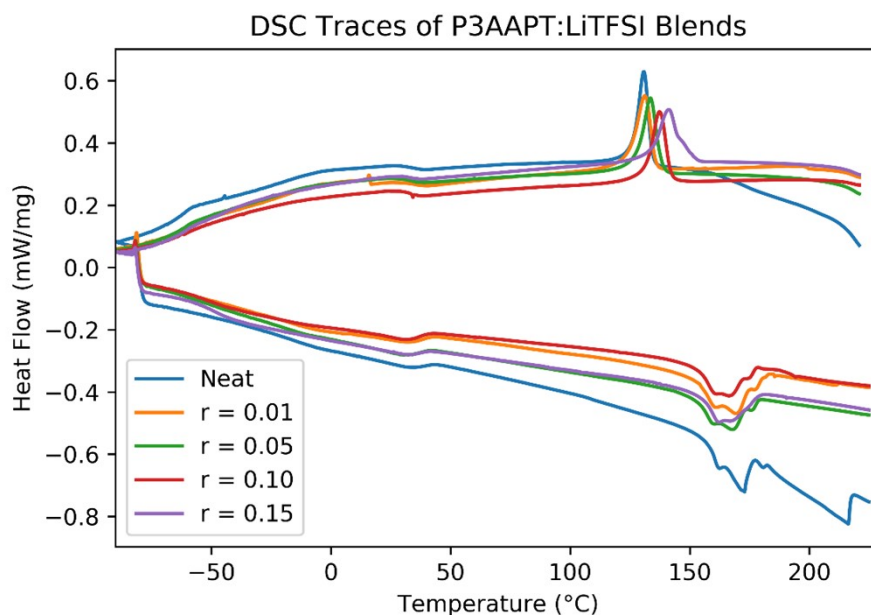


Figure S8: Differential scanning calorimetry, DSC, Traces of P3AAPT:LiTFSI. Shown data is from the cooling cycle and the second heating cycle. Traces are vertically offset for added clarity. The weak endotherm near 30 °C upon heating is attributed to a side chain melt, while the complex structure between 150 °C and 175 °C is attributed to the main chain melt, complicated by either crystal size dispersion or crystal polymorph. Exothermic up.

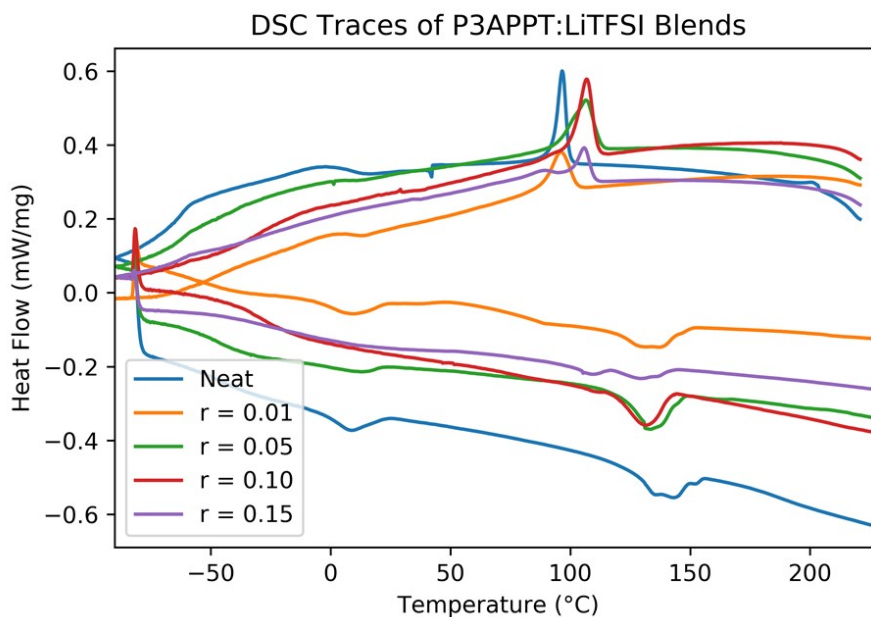


Figure S9: DSC Traces of P3APPT:LiTFSI. Shown data is from the cooling cycle and the second heating cycle. Traces are vertically offset for added clarity. The weak endotherm near 10 °C upon heating is attributed to a side chain melt, while the complex structure between 110 °C and 150 °C is attributed to the main chain melt, complicated by either crystal size dispersion or crystal polymorph. Additional melting and crystallizing thermal transitions are observed at 110 °C and 90 °C, respectively, at LiTFSI concentrations of $r = 0.15$. Exothermic up.

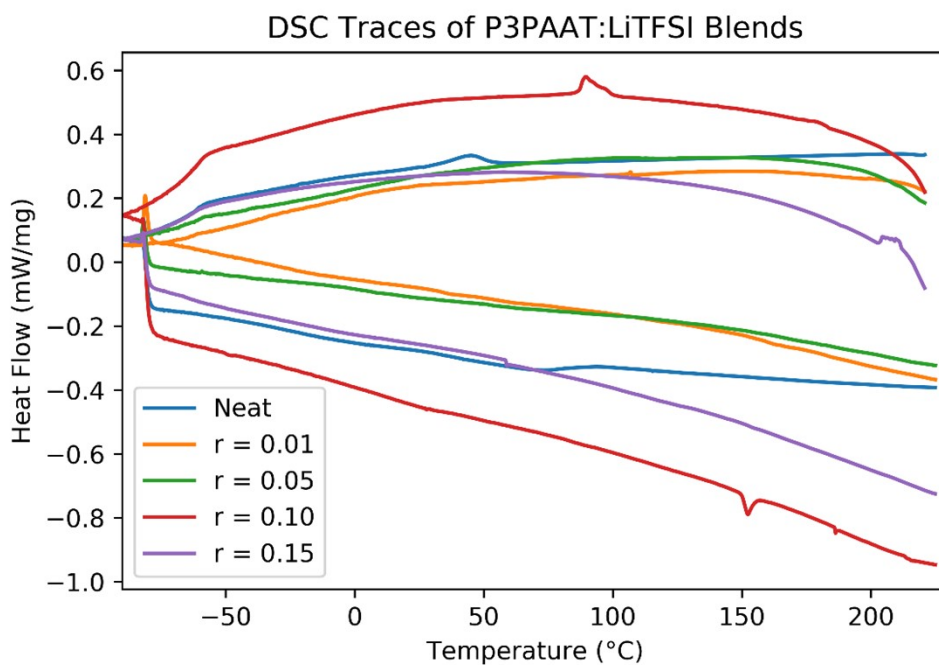


Figure S10: DSC Traces of P3PAAT:LiTFSI. Shown data is from the cooling cycle and the second heating cycle. Traces are vertically offset for added clarity. The weak thermal transition around 50 °C in the neat sample is attributed to a side chain melting. Exothermic up.

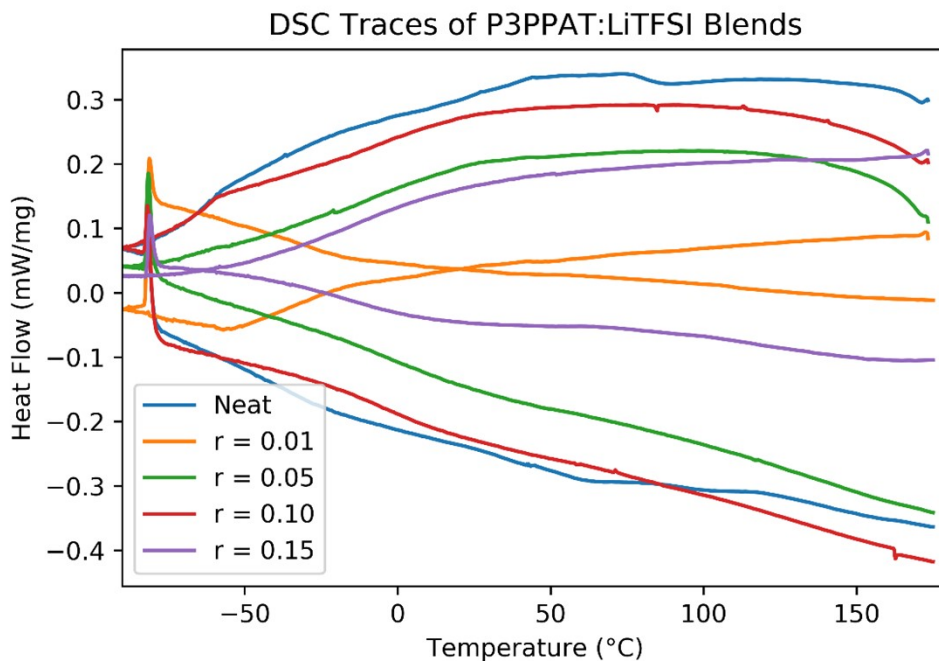


Figure S11: DSC Traces of P3PPAT:LiTFSI. Shown data is from the cooling cycle and the second heating cycle. Traces are vertically offset for added clarity. Exothermic up.

Table S1: Summary of thermal transitions observed in DSC traces for all polymers. N/A is used to indicate that no thermal transition was visible. * Data acquisition trace had a machine blip during run – value not reportable. †Backbone signal was split, the results of which are reported as lower transition/higher transition.

Polymer	LiTFSI	Side Chain				Backbone			
		r	T_m (°C)	ΔH_f (J/g)	T_c (°C)	ΔH_f (J/g)	T_m (°C)	ΔH_f (J/g)	T_c (°C)
P3AAPT	0	34	1.6	26	0.4	172	9.2	131	10.5
	0.01	32	2.1	18	*	170	14.3	132	11.7
	0.05	29	2.0	25	1.5	168	11.2	134	11.4
	0.10	32	1.6	30	1.3	166	9.7	138	10.4
	0.15	31	1.5	28	1.4	165	9.8	142	11.2
P3APPT	0	-3	3.9	8	3.3	144	7.5	97	7.6
	0.01	8	3.5	-2	2.2	138	6.8	97	7.1
	0.05	14	1.4	-2	1.2	135	9.7	106	8.9
	0.10	N/A	N/A	N/A	N/A	132	7.2	107	10.3
	0.15 [†]	N/A	N/A	N/A	N/A	108/132	1.1/2.0	88/106	0.6/2.2
P3PAAT	0	70	2.2	45	2.9	N/A	N/A	N/A	N/A
	0.01	N/A	N/A	N/A	N/A	N/A	N/A	N/A	N/A
	0.05	N/A	N/A	N/A	N/A	N/A	N/A	N/A	N/A
	0.10	N/A	N/A	N/A	N/A	152	0.2	92	0.5
	0.15	N/A	N/A	N/A	N/A	N/A	N/A	N/A	N/A
P3PPAT	0	N/A	N/A	N/A	N/A	N/A	N/A	N/A	N/A
	0.01	N/A	N/A	N/A	N/A	N/A	N/A	N/A	N/A
	0.05	N/A	N/A	N/A	N/A	N/A	N/A	N/A	N/A
	0.10	N/A	N/A	N/A	N/A	N/A	N/A	N/A	N/A
	0.15	N/A	N/A	N/A	N/A	N/A	N/A	N/A	N/A

S.3. Ultraviolet-Visible, UV-Vis, Analysis

Calculations for Table S2 were performed by taking the intensity ratios of the local extrema for the different peak components for all doping levels for P3AAPT and P3APPT. The relative change is small across doping levels; however, it shows an improvement in backbone planarization and

close packing of polymer chains with increasing A_{0-0}/A_{0-1} ratio. Due to the lack of an apparent vibronic progression for P3PAAT and P3PPAT, an A_{0-0}/A_{0-1} ratio is not applicable for those polymers.

Table S2: A_{0-0}/A_{0-1} intensity ratios, absorption onsets, and absorption maxima for all polymer:LiTFSI blends.

LiTFSI Level:		Neat	$r = 0.01$	$r = 0.05$	$r = 0.10$	$r = 0.15$
P3AAPT	A_{0-0}/A_{0-1}	0.73	0.79	0.78	0.81	0.79
P3APPT	A_{0-0}/A_{0-1}	0.71	0.75	0.77	0.73	0.72
P3AAPT	λ_{onset} (nm)	663	662	664	657	659
P3APPT	λ_{onset} (nm)	657	664	660	660	661
P3PAAT	λ_{onset} (nm)	575	570	570	572	574
P3PPAT	λ_{onset} (nm)	580	590	610	605	595
P3AAPT	λ_{max} (nm)	557	555	555	555	553
P3APPT	λ_{max} (nm)	550	550	550	549	547
P3PAAT	λ_{max} (nm)	466	462	465	464	466
P3PPAT	λ_{max} (nm)	473	472	482	485	470

S.4. Grazing Incidence Wide-Angle X-Ray Scattering, GIWAXS, Supplemental Data

All values contained within Table S3 and Table S4 are the results of fits to the relevant line traces using a sum of Gaussian, Lorentzian, or pseudo-Voigt peaks, after an asymmetric least squares background filter was applied. The reported uncertainty in peak positions and FWHM is a combination of the standard deviation from the peak fitting, combined with a 0.002 \AA^{-1} approximation for the combined influence of correcting for refractive index and distorted Born wave approximation (DBWA) contributions. The uncertainties for d-spacing and swelling (percent change) are derived from the peak position uncertainties by propagating error. For the out-of-plane (h00) series, we report an average $d_{100} \equiv \langle h^*d_{h00} \rangle$ where $\langle \rangle$ is the uncertainty weighted average of the three observed orders.

Table S3: Full summary data of GIWAXS experiments for all polymers and LiTFSI concentrations.

P3AAPT							
	LiTFSI content	$r =$	0	0.01	0.05	0.1	0.15
Reciprocal Space Peak Position (q)	Out of plane (100)	(\AA^{-1})	0.287 ± 0.002	0.280 ± 0.002	0.272 ± 0.002	0.261 ± 0.002	0.252 ± 0.002
	Out of plane (200)	(\AA^{-1})	0.579 ± 0.004	0.567 ± 0.003	0.554 ± 0.003	0.539 ± 0.003	0.519 ± 0.002

	Out of plane (300)	(\AA^{-1})	0.871 ± 0.009	0.856 ± 0.007	0.835 ± 0.005	0.823 ± 0.004	0.813 ± 0.004
	Out of plane π	(\AA^{-1})	1.67 ± 0.09	1.70 ± 0.09	1.68 ± 0.09	1.67 ± 0.02	1.68 ± 0.02
	In plane (100)	(\AA^{-1})	0.286 ± 0.002	0.284 ± 0.002	0.275 ± 0.002	0.269 ± 0.002	0.259 ± 0.002
	In plane π	(\AA^{-1})	1.672 ± 0.004	1.672 ± 0.004	1.672 ± 0.004	1.674 ± 0.004	1.678 ± 0.005
Real Space d-spacing	Out of plane (100)	(\AA)	21.9 ± 0.2	22.4 ± 0.2	23.1 ± 0.2	24.1 ± 0.2	24.9 ± 0.2
	Out of plane (200)	(\AA)	10.9 ± 0.1	11.1 ± 0.1	11.3 ± 0.1	11.7 ± 0.1	12.1 ± 0.1
	Out of plane (300)	(\AA)	7.21 ± 0.07	7.34 ± 0.06	7.53 ± 0.05	7.63 ± 0.04	7.73 ± 0.04
	Average d_{100}	(\AA)	21.8 ± 0.1	22.2 ± 0.1	22.7 ± 0.1	23.2 ± 0.1	23.8 ± 0.1
	Out of plane π	(\AA)	3.77 ± 0.20	3.71 ± 0.20	3.75 ± 0.20	3.76 ± 0.05	3.74 ± 0.04
	In plane (100)	(\AA)	22.0 ± 0.2	22.1 ± 0.2	22.8 ± 0.2	23.4 ± 0.2	24.3 ± 0.2
	In plane π	(\AA)	3.74 ± 0.01	3.76 ± 0.01	3.76 ± 0.01	3.75 ± 0.01	3.74 ± 0.01
P3APPT							
	LiTFSI content	$r =$	0	0.01	0.05	0.1	0.15
Reciprocal Space Peak Position (q)	In plane (100)	(\AA^{-1})	0.319 ± 0.002	0.314 ± 0.002	0.293 ± 0.002	0.281 ± 0.002	0.276 ± 0.002
	In plane (200)	(\AA^{-1})	0.638 ± 0.004	0.624 ± 0.004	0.581 ± 0.002	0.558 ± 0.002	0.546 ± 0.005
	In plane (300)	(\AA^{-1})	0.946 ± 0.005	0.938 ± 0.004	0.867 ± 0.004	0.835 ± 0.002	0.820 ± 0.002
	In plane π	(\AA^{-1})	1.666 ± 0.004	1.673 ± 0.004	1.671 ± 0.006	N/A	N/A

	Out of plane (100)	(\AA^{-1})	0.320 ± 0.002	0.316 ± 0.002	0.285 ± 0.002	0.287 ± 0.003	N/A
	Out of plane π	(\AA^{-1})	1.687 ± 0.009	1.690 ± 0.009	1.691 ± 0.006	1.681 ± 0.004	1.638 ± 0.004
Real Space d-spacing	In plane (100)	(\AA)	19.7 ± 0.1	20.0 ± 0.1	21.4 ± 0.1	22.4 ± 0.2	22.8 ± 0.2
	In plane (200)	(\AA)	9.85 ± 0.06	10.1 ± 0.1	10.8 ± 0.1	11.3 ± 0.1	11.5 ± 0.1
	In plane (300)	(\AA)	6.64 ± 0.04	6.70 ± 0.03	7.25 ± 0.03	7.52 ± 0.02	7.66 ± 0.02
	Average d_{100}	(\AA)	19.8 ± 0.06	20.1 ± 0.06	21.6 ± 0.06	22.6 ± 0.06	23.0 ± 0.06
	In plane π	(\AA)	3.77 ± 0.01	3.76 ± 0.01	3.76 ± 0.01	N/A	N/A
	Out of plane (100)	(\AA)	19.6 ± 0.1	19.9 ± 0.1	22.0 ± 0.2	22.0 ± 0.3	N/A
	Out of plane π	(\AA)	3.72 ± 0.02	3.72 ± 0.02	3.72 ± 0.01	3.74 ± 0.01	3.84 ± 0.01

P3PAAT							
	LiTFSI content	$r =$	0	0.01	0.05	0.1	0.15
Reciprocal Space Peak Position (q)	Out of plane (100)	(\AA^{-1})	0.307 ± 0.002	0.309 ± 0.002	0.286 ± 0.002	0.287 ± 0.002	0.287 ± 0.002
	Out of plane (200)	(\AA^{-1})	0.613 ± 0.009	0.612 ± 0.009	0.583 ± 0.008	0.593 ± 0.008	0.595 ± 0.006
	Out of plane (300)	(\AA^{-1})	0.91 ± 0.02	0.91 ± 0.02	0.88 ± 0.02	0.88 ± 0.02	0.87 ± 0.01
	Out of plane π	(\AA^{-1})	N/A	N/A	N/A	1.593	N/A
	In plane (100)	(\AA^{-1})	0.306 ± 0.002	0.305 ± 0.002	0.291 ± 0.002	0.294 ± 0.002	0.295 ± 0.002

	In plane π	(\AA^{-1})	1.651 ± 0.006	1.656 ± 0.008	1.639 ± 0.009	1.63 ± 0.01	N/A
Real Space d-spacing	Out of plane (100)	(\AA)	20.5 ± 0.1	20.3 ± 0.1	22.0 ± 0.2	21.9 ± 0.2	21.9 ± 0.2
	Out of plane (200)	(\AA)	10.3 ± 0.2	10.3 ± 0.2	10.8 ± 0.1	10.6 ± 0.1	10.6 ± 0.1
	Out of plane (300)	(\AA)	6.91 ± 0.15	6.91 ± 0.15	7.14 ± 0.16	7.14 ± 0.16	7.22 ± 0.08
	Average d_{100}	(\AA)	20.5 ± 0.09	20.3 ± 0.09	21.8 ± 0.1	21.5 ± 0.1	21.6 ± 0.1
	Out of plane π	(\AA)	N/A	N/A	N/A	3.944	N/A
	In plane (100)	(\AA)	20.5 ± 0.1	20.6 ± 0.1	21.6 ± 0.1	21.4 ± 0.1	21.3 ± 0.1
	In plane π	(\AA)	3.81 ± 0.01	3.80 ± 0.02	3.83 ± 0.02	3.85 ± 0.02	N/A

P3PPAT							
	LiTFSI content	$r =$	0	0.01	0.05	0.1	0.15
Reciprocal Space Peak Position (q)	Out of plane (100)	(\AA^{-1})	0.304 ± 0.002	0.298 ± 0.002	0.289 ± 0.002	0.278 ± 0.002	0.275 ± 0.002
	Out of plane (200)	(\AA^{-1})	0.610 ± 0.008	0.603 ± 0.008	0.59 ± 0.01	N/A	N/A
	Out of plane (300)	(\AA^{-1})	0.918 ± 0.008	0.910 ± 0.008	0.89 ± 0.01	0.87 ± 0.01	0.85 ± 0.01
	Out of plane π	(\AA^{-1})	1.65 ± 0.03	1.64 ± 0.01	1.64 ± 0.01	1.63 ± 0.01	1.63 ± 0.03
	In plane (100)	(\AA^{-1})	0.301 ± 0.002	0.302 ± 0.002	0.293 ± 0.002	0.287 ± 0.002	0.284 ± 0.002
	In plane π	(\AA^{-1})	1.640 ± 0.007	N/A	N/A	N/A	N/A

Real Space d-spacing	Out of plane (100)	(Å)	20.7 ± 0.1	21.1 ± 0.1	21.7 ± 0.2	22.6 ± 0.2	22.8 ± 0.2
	Out of plane (200)	(Å)	10.3 ± 0.1	10.4 ± 0.1	10.7 ± 0.2	N/A	N/A
	Out of plane (300)	(Å)	6.85 ± 0.06	6.91 ± 0.06	7.06 ± 0.08	7.22 ± 0.08	7.40 ± 0.09
	Average d ₁₀₀	(Å)	20.6 ± 0.08	21.0 ± 0.08	21.5 ± 0.1	22.2 ± 0.1	22.6 ± 0.2
	Out of plane π	(Å)	3.81 ± 0.07	3.83 ± 0.02	3.83 ± 0.02	3.85 ± 0.02	3.86 ± 0.07
	In plane (100)	(Å)	20.9 ± 0.1	20.8 ± 0.1	21.4 ± 0.1	21.9 ± 0.2	22.1 ± 0.2
	In plane π	(Å)	3.83 ± 0.02	N/A	N/A	N/A	N/A

To offer another perspective on changes in d-spacing with LiTFSI introduction, a percent swelling calculation was performed for the (100) and (010) directions. The calculation was performed using a percent change equation for each peak, Percent Swelling = $(l - l_o)/l_o * 100\%$, where the l is the d-spacing, and l_o is the neat polymer d-spacing. The results of these calculations for all polymers is shown in Table S4.

Table S4: Percent swelling for the (100) and (010) planes of all polymers with LiTFSI introduction.

Percent Swelling, P3AAPT	LiTFSI Content, $r =$		0	0.01	0.05	0.1	0.15
	(100)	(%)	0	2.3 ± 1.8	5.5 ± 1.9	10 ± 2	14 ± 2
	(010)	(%)	0	0.54 ± 0.54	0.54 ± 0.54	0.27 ± 0.54	0 ± 0.54
Percent Swelling, P3APPT	LiTFSI Content, $r =$		0	0.01	0.05	0.1	0.15
	(100)	(%)	0	1.5 ± 1.0	8.6 ± 1.1	14 ± 2	16 ± 2
	(010)	(%)	0	0.0 ± 1.1	0.0 ± 0.8	0.5 ± 0.8	3.2 ± 0.8
Percent Swelling, P3PAAT	LiTFSI Content, $r =$		0	0.01	0.05	0.1	0.15
	(100)	(%)	0	1.0 ± 1.0	7.3 ± 1.5	6.8 ± 1.5	6.8 ± 1.5
	(010)	(%)	0	-0.3 ± 0.8	0.5 ± 0.8	1.1 ± 0.8	N/A
Percent	LiTFSI Content, $r =$		0	0.01	0.05	0.1	0.15

Swelling, P3PPAT	(100)	(%)	0	1.9 ± 1.0	4.8 ± 1.5	9.2 ± 1.5	10.2 ± 1.5
	(010)	(%)	0	0.6 ± 2.4	0.6 ± 2.4	1.1 ± 2.4	1.3 ± 3.7

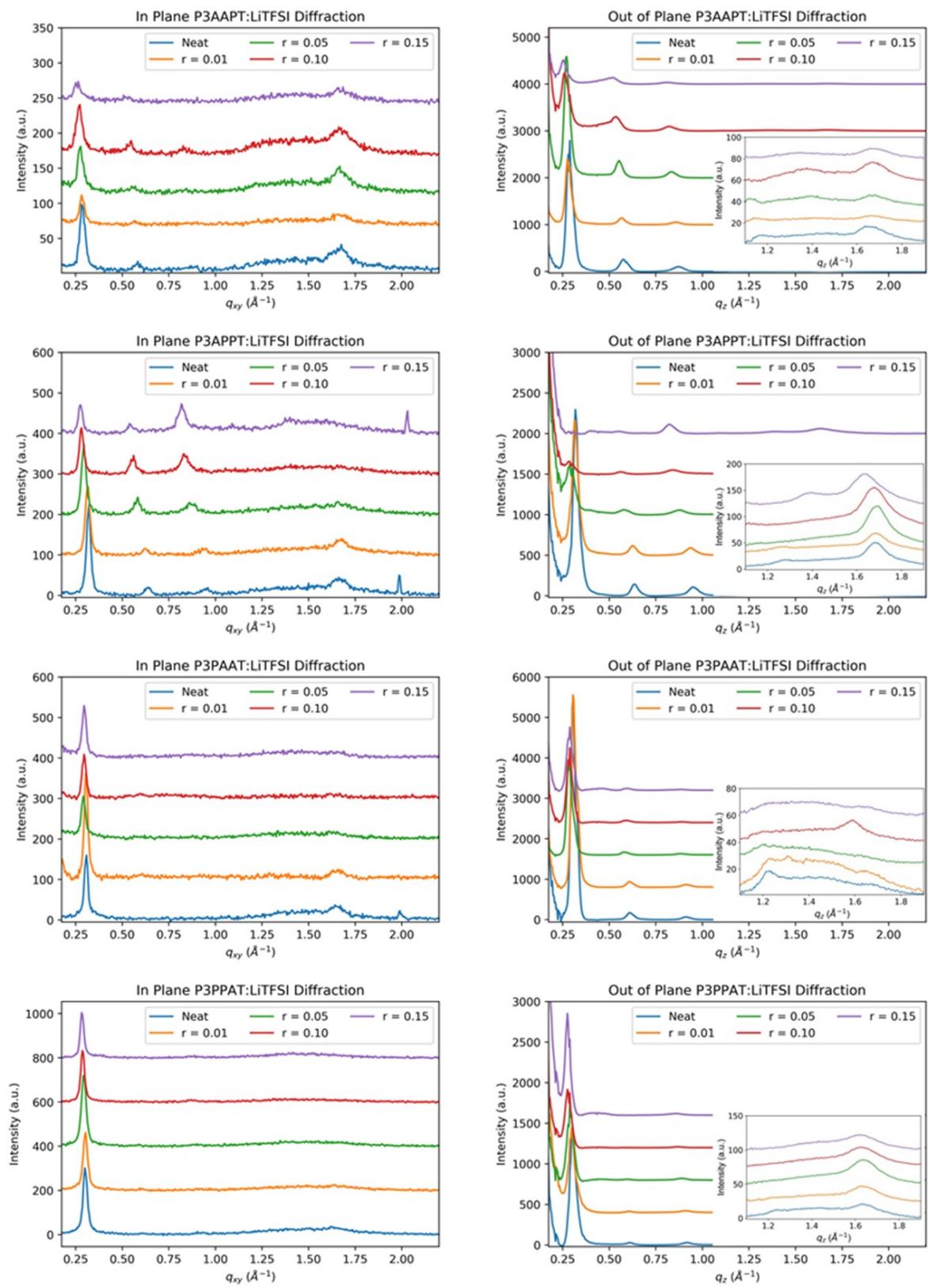
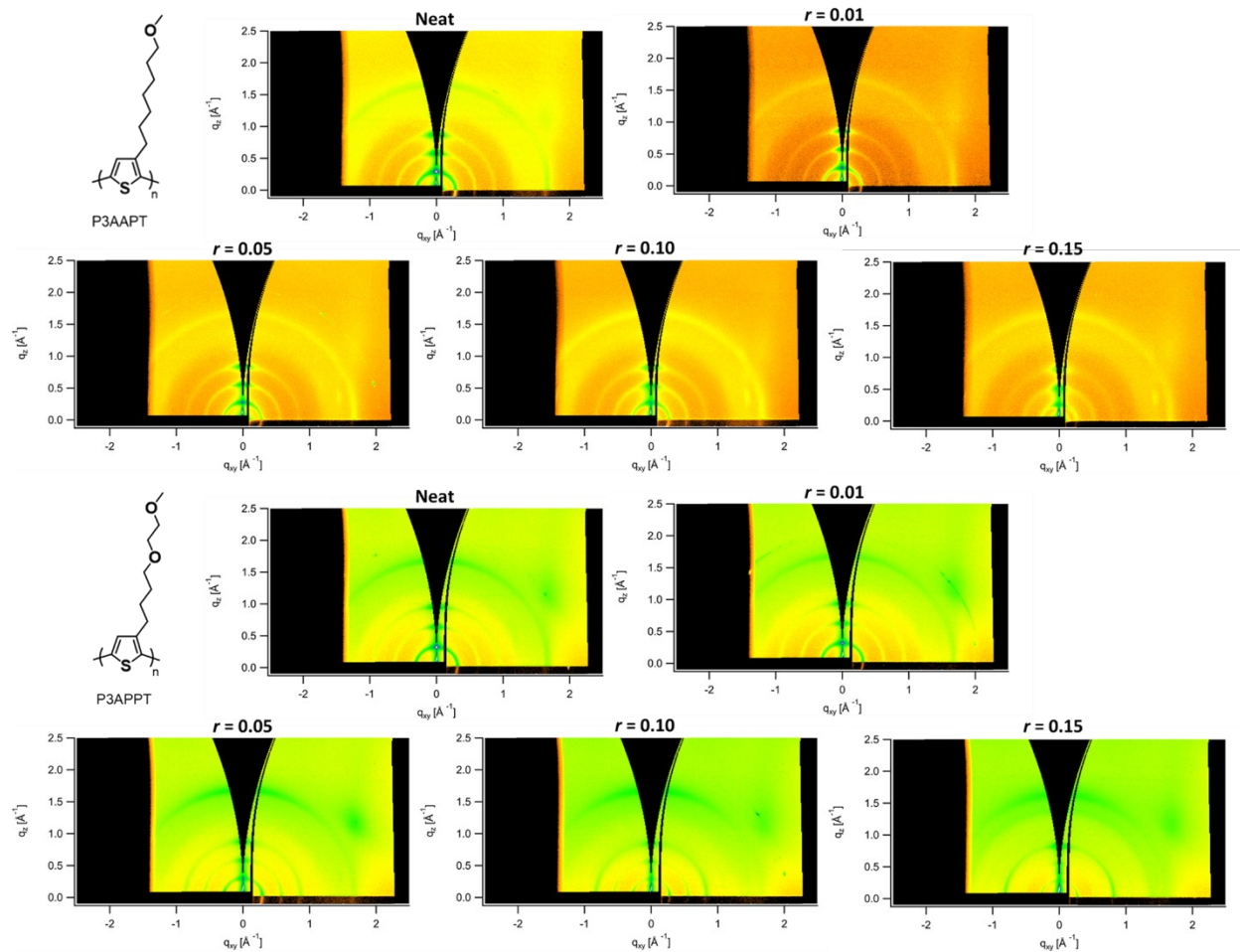


Figure S12: GIWAXS linecuts in and out of plane for all polymers across all LiTFSI concentrations.

The 2-D diffraction data is also presented in Figure S13 for all polymers for completeness.



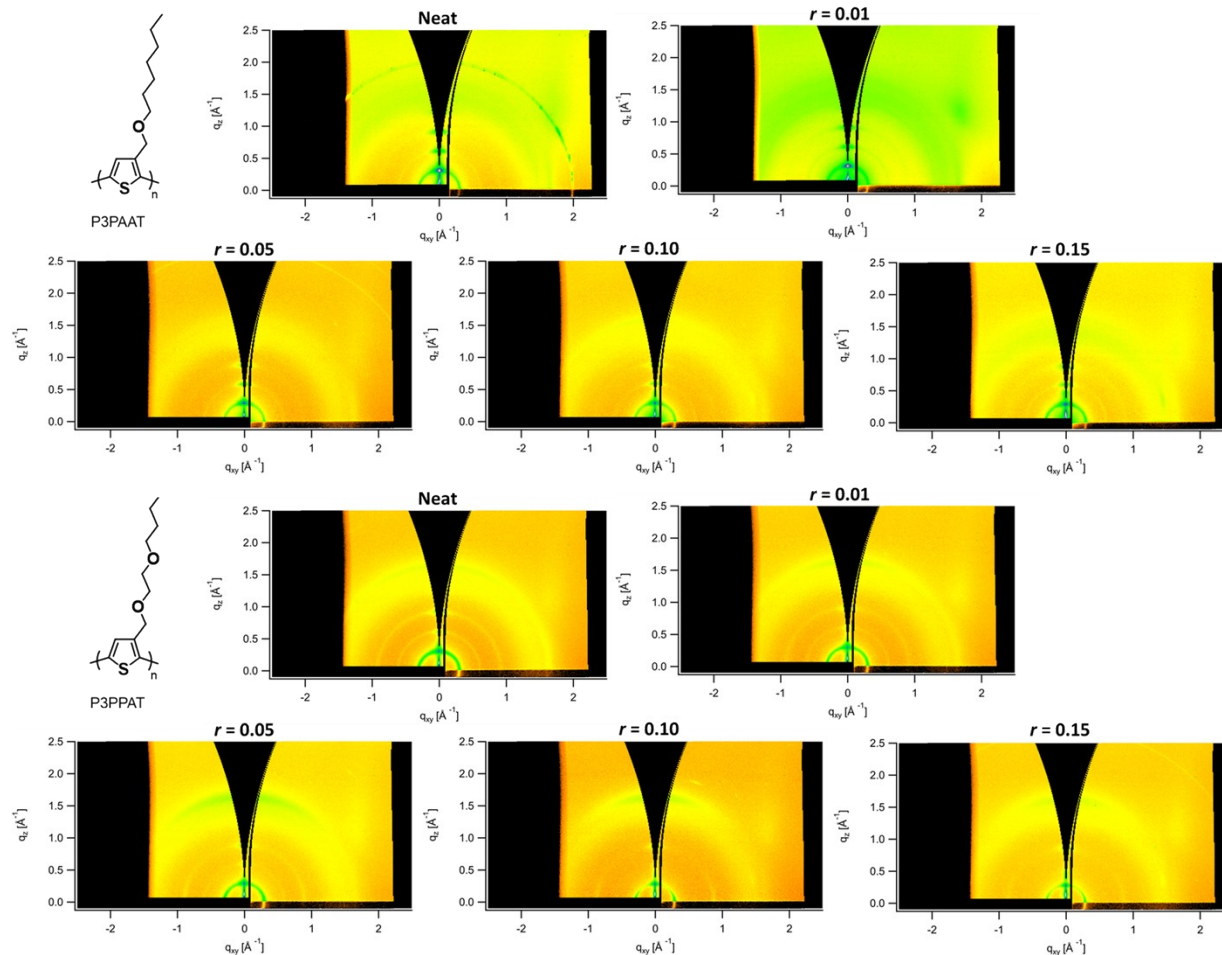
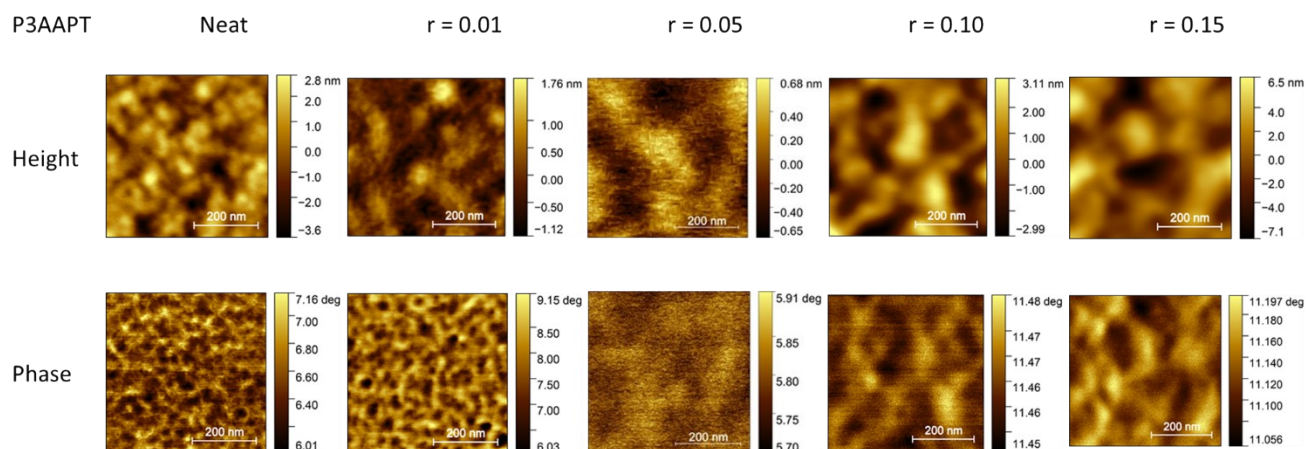


Figure S13: 2D GIWAXS diffractograms for all polymers and LiTFSI concentrations.

S.5. Atomic Force Microscopy



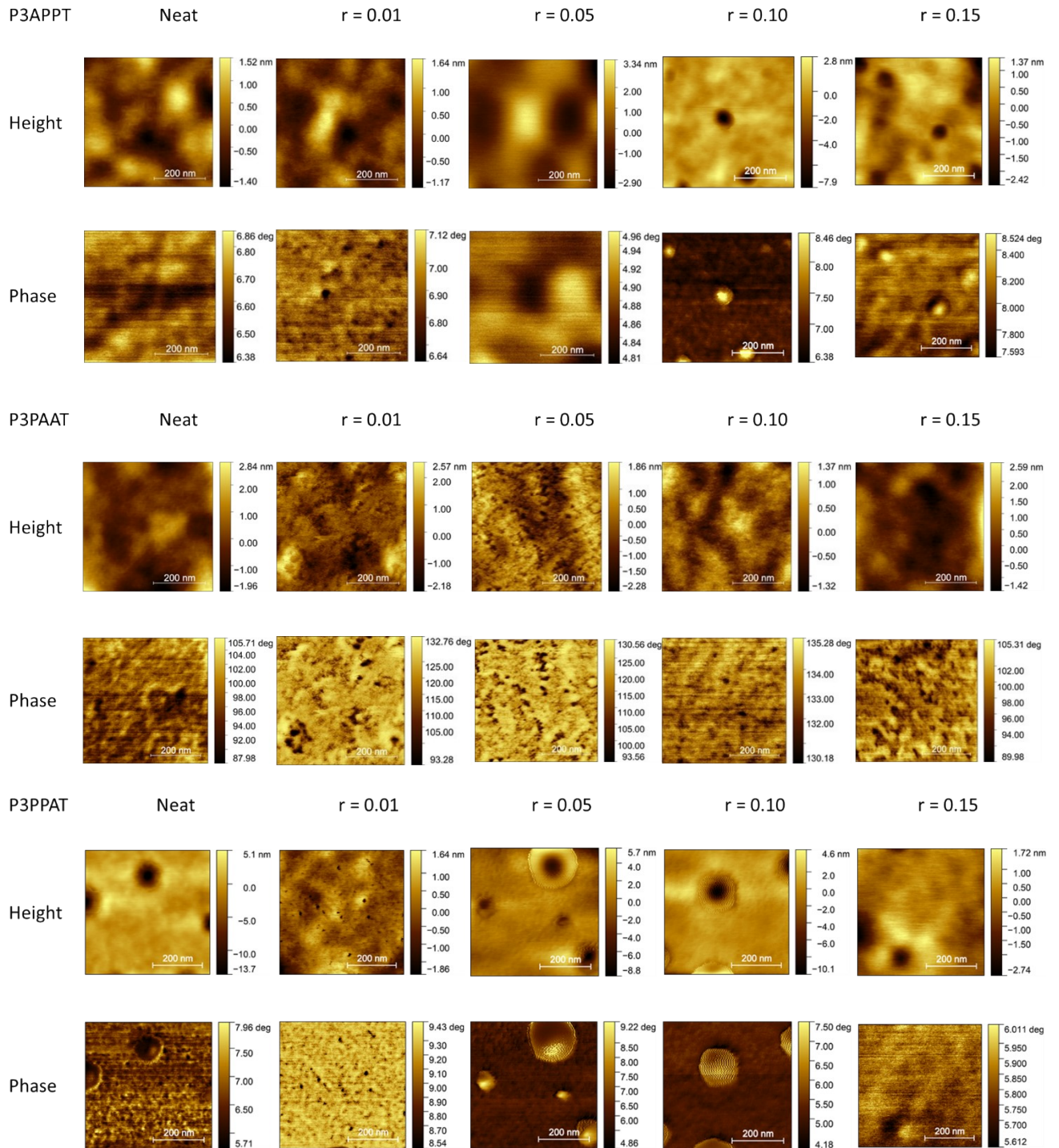


Figure S14: AFM height and phase data for all neat and polymer:LiTFSI blends.

S.6. Molecular Dynamics

S.6.1 Force Field Parameters

The force field employed in this work was previously used in the study of P3MEEMT.² In this model, the all-atom force field developed by Huang *et al.*³ is used to simulate the polythiophene backbones, while the optimized potentials for liquid simulations-all atoms (OPLS-AA) forcefield⁴ is adopted to simulate various side chains as described in the main text. Partial charges of the thiophene atoms were reparameterized using BLYP 6-31G*.² The torsional potentials between ring-ring and ring-sidechain atoms were found from Poelking *et al.*,⁵ and their parameter set is defined by Equation S1, $\{C_n\}$. To implement the dihedral potential of the Poelking *et al.*⁵ model into the LAMMPS simulation package,⁶ we define a new parameter set using Equation S2, $\{K_n\}$ and $\alpha_n = 0$. The relation between two parameter sets, $\{C_n\}$ and $\{K_n\}$, can be determined through tedious trigonometric transformations, the result of which is shown in Equation S3. For the lithium salt, the OPLS-AA forcefield⁴ is used to simulate Li^+ , while the all-atom force field developed by Lopes *et al.*⁷ is used to simulate TFSI.

$$V_{MH}(\phi) = \sum_{n=0}^5 C_n \cos^n \phi \text{ Equation S1}$$

$$V_F(\phi) = \sum_{n=0}^5 K_n [1 + \cos(n\phi - \alpha_n)], \alpha_n = 0. \text{ Equation S2}$$

$$A_0 = C_0 + \frac{1}{8}(4C_2 + 3C_4) \text{ Equation S3a}$$

$$K_1 = \frac{1}{8}(8C_1 + 6C_3 + 5C_5) \text{ Equation S3b}$$

$$K_2 = \frac{1}{2}(C_2 + C_4) \text{ Equation S3c}$$

$$K_3 = \frac{1}{16}(4C_3 + 5C_5) \text{ Equation S3d}$$

$$K_4 = \frac{1}{8}C_4 \text{ Equation S3e}$$

$$K_5 = \frac{1}{16}C_5 \text{ Equation S3f}$$

$$K_0 = \frac{1}{2}(A_0 - K_1 - K_2 - K_3 - K_4 - K_5) \text{ Equation S3g}$$

The force field parameters of each type of polymer studied in this work are included in a compressed folder, “forceField.zip”. To facilitate reproducing our simulation work, three files are usually provided for each polymer type. Below, we will use P3APPT as an example to explain in detail the information provided.

S.6.1.1 Image File: “Chemical-map.png”

This image file is shown in Figure S15. The definition of atom types is a key factor to introduce to a force field. Figure S15 illustrates the definition of each atom type within the molecule along the polymer backbone. There could be several atom types for the same element. For example, carbon atoms can be grouped into three different atom types, $\{C_A, C_T, C_S\}$. Each polymer chain can contain various numbers of repeat units. To avoid redundant information, we use an oligomer of four repeat units to illustrate the force field of P3APPT. Figure S15 also shows the relative position of each atom in the molecule. Each atom is represented by its type and ID. For example, “C_{A20}” stands for the carbon atom of *atomType*=C_A and *atomID*=20. For clarity, we omit most of the hydrogen atoms, though the full list of atoms can be found in another .txt file, “atom-info.txt”. The rule of thumb to learn the position of hydrogen atom is the following: the *atomID* of each hydrogen atom follows right after the atom they attached. For example, “C_{T11}” is a carbon atom of *atomID*=11, “H_{C12}” and “H_{C13}” are two hydrogen atoms of *atomID*=12 and *atomID*=13 right after 11. Then “H_{C12}” and “H_{C13}” attach to “C_{T11}”. Similarly, “H_{A4}” attaches to “C_{A3}”. “H_{C15}” and “H_{C16}” attach to “C_{T14}”. “H_{C29}”, “H_{C30}” and “H_{C31}” attach to “C_{T28}”.

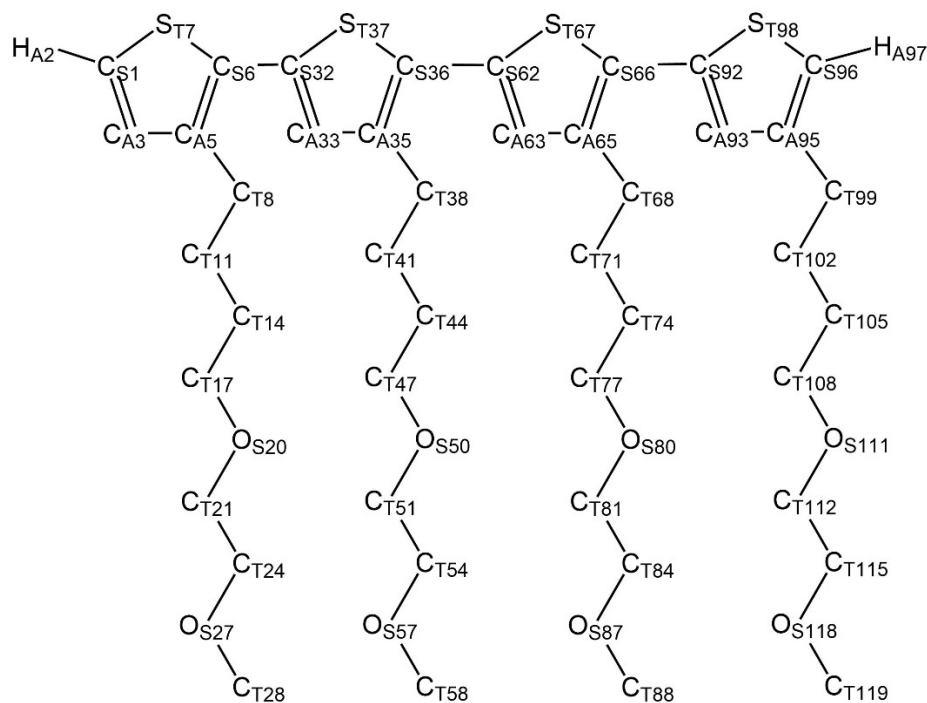


Figure S15: Chemical structure of a four-repeat-unit oligomer of the P3APPT polymer. Atoms of different types in our atomistic model are labeled with different letter subscripts. Each atom is also labeled with a numerical subscript to indicate its atomID. Noted that the numerical subscript is not consecutive, and missing numbers represent omitted hydrogen atoms for the clarity of illustration.

S.6.1.2 Text File: “atom-info.txt”

This file contains all the geometric information of the four-repeat-unit oligomer of P3APPT. We will go through every section to explain the information contained; namely, the number of atom types, bond type, angle type and dihedral type in the force field. It also provides the number of atoms, bonds, angles, and dihedrals in this oligomer.

Atom type. A *number* and a *keyword* are used to define each atom type. The *number* is mainly used for simulation software (e.g., LAMMPS). The *keyword* contains the chemical element (e.g., C, H, O) and a customized label to differentiate various atom type of the same chemical element. The chemical meaning of each atom type can be found in the image file, “Chemical-map.png”.

Masses. This section gives the mass of each atom type. The *number* in each line is defined in the atom type section.

Bond type. A *number* and a *keyword* are used to define each bond type. The *number* is mainly used for simulation software (e.g., LAMMPS). The *keyword* contains two *atom-type-keyword*.

Angle type. A *number* and a *keyword* are used to define each angle type. The *number* is mainly used for simulation software (e.g., LAMMPS). The *keyword* contains three *atom-type-keyword*.

Dihedral type. A *number* and a *keyword* are used to define each dihedral type. The *number* is mainly used for simulation software (e.g., LAMMPS). The *keyword* contains four *atom-type-keyword*.

Atom. This section defines a list of atoms. Each atom is provided with six items, including *atomID*, *atomType*, *q*, *x*, *y*, *z*. *atomID* is consistent with the image file, “Chemical-map.png”. *atomType* is the number defined in the atom type section. *q* is the charge of the atom. *x y z* are the coordinates of the atom for illustration purpose.

Bond. This section defines a list of bonds. Each bond is provided with four items, including *bondID*, *bondType*, *atomID1*, *atomID2*. *bondType* is the number defined in the bond type section. *atomID1* and *atomID2* tells which two atoms form this bond.

Angle. This section defines a list of bending angles. Each angle is provided with five items, including *angleID*, *angleType*, *atomID1*, *atomID2*, *atomID3*. *angleType* is the number defined in the angle type section. *atomID1*, *atomID2* and *atomID3* tells which three atoms form this angle.

Dihedral. This section defines a list of dihedrals. Each dihedral is provided with six items, including *dihedralID*, *dihedralType*, *atomID1*, *atomID2*, *atomID3*, *atomID4*. *dihedralType* is the number defined in the dihedral type section. *atomID1*, *atomID2*, *atomID3* and *atomID4* tells which four atoms form this dihedral.

This text file only contains the information of four repeat units. However, the second unit (from *atomID*=32 to *atomID*=61) and the third unit (from *atomID*=62 to *atomID*=91) can be duplicated several times to generate polymer chains with the desired lengths.

S.6.1.3 Text File: “forcefield-lammps.txt”

This file contains all parameters of the force field. It is written in the LAMMPS style. The units of each parameter and the functional form of each potential are well-defined in the LAMMPS website. We briefly summarize in the equation set, Equation S4. For more information, please visit LAMMPS website (lammps.sandia.gov).

$$U_{LJ} = 4\epsilon \left[\left(\frac{\sigma}{r} \right)^{12} - \left(\frac{\sigma}{r} \right)^6 \right], \epsilon: kcal \cdot mol^{-1}, \sigma: \text{\AA}. \text{ Equation S4a}$$

$$U_{bond} = K(r - r_0)^2, K: kcal \cdot mol^{-1} \cdot \text{\AA}^{-2}, r_0: \text{\AA}. \text{ Equation S4b}$$

$$U_{angle} = K(\theta - \theta_0)^2, K: kcal \cdot mol^{-1} \cdot rad^{-2}, \theta_0: ^\circ. \text{ Equation S4c}$$

$$U_{dihed-OPLS} = \sum_{n=1}^4 \frac{1}{2} K_n [1 + (-1)^{n+1} \cos(n\phi)], K_n: kcal \cdot mol^{-1}. \text{ Equation S4d}$$

$$U_{dihed-Fourier} = \sum_{n=0}^5 K_n [1 + \cos(n\phi - \alpha_n)], K_n: kcal \cdot mol^{-1}. \text{ Equation S4e}$$

S.6.2 Structure Generation

For each polymer species, crystalline and amorphous morphologies were investigated. The procedure to generate targeted morphology is described in the following section. This procedure is developed based on the LAMMPS software and only serves as a reference as other approaches could also be used.

S.6.2.1 Crystalline Morphology

The polymorph I of poly(3-hexylthiophene) (P3HT) is used as a template.⁸ The unit cell of this polymorph contains two chains with lattice parameter ($a = 16 \text{ \AA}$, $b = 7.8 \text{ \AA}$, $c = 7.8 \text{ \AA}$, $\alpha = 90^\circ$, $\beta = 90^\circ$, $\gamma = 86.5^\circ$). To accommodate larger side chains of each polymer, we usually adopt a unit cell with elongated a -dimension. Fig. S16(a) shows an example of generated crystalline template of

P3APPT with $a_{\text{new}} = 22 \text{ \AA}$. In this template, each polymer chain contains ten repeat units, eight chains form a layer, and two layers form the lamella phase. This template is fitted into a tetragonal simulation box by applying the periodic boundary condition with the box dimension ($L_x = 5c = 39 \text{ \AA}$, $L_y = 4b = 31.2 \text{ \AA}$, $L_z = 2a_{\text{new}} \cdot \sin \gamma = 43.92 \text{ \AA}$). The coordinates of thiophene atoms are taken directly from the polymorph I of P3HT. The larger side chain with various chemical composition can be pre-generated with reasonable configuration (no unphysical geometry) by other software and attached to each thiophene ring through some additional ad-hoc translational and rotational manipulation. Furthermore, we can add one layer of LiTFSI salt to simulate the dissociation process with a larger box length in z -axis, $L_{z,I} = 57.94 \text{ \AA}$. We include a LAMMPS trajectory file of such crystalline template in the compressed folder, “forceField.zip”.

The crystalline template described above serves as the initial configuration. To fit our simulation purpose, we propose several constraints for the equilibrated crystalline morphology. The polythiophene backbone should remain the same as that of polymorph I of P3HT with fixed position during simulation, and servers as anchors for side chains. Side chains should be fully equilibrated to form a disordered region to interact with LiTFSI salt. One example of such equilibrated crystalline morphology is shown in Fig. S16(b). Compared with the template, only the box length in the z -axis (L_z) is changed to equilibrate the system. We pre-run some isothermal-isobaric ensemble (NPT) simulations with barostat coupling only to the z -axis for each polymer species to simulate the condition of 1 atm at the target simulation temperature (*e.g.*, 400 K). An average value of L_z among all species is calculated. The final box dimension of all species is $L_{z,f} = 43.206 \text{ \AA}$ for 400 K; this setup is convenient to compare local oxygen concentration across different species. Using a universal value of L_z may over- or under-estimate the pressure in some species. However, with similar chemical composition among species, this mismatch has very

limited effects, and does not change the general trend we found regarding of the dissociation free energy, which is confirmed by our additional simulations (not included in the SI).

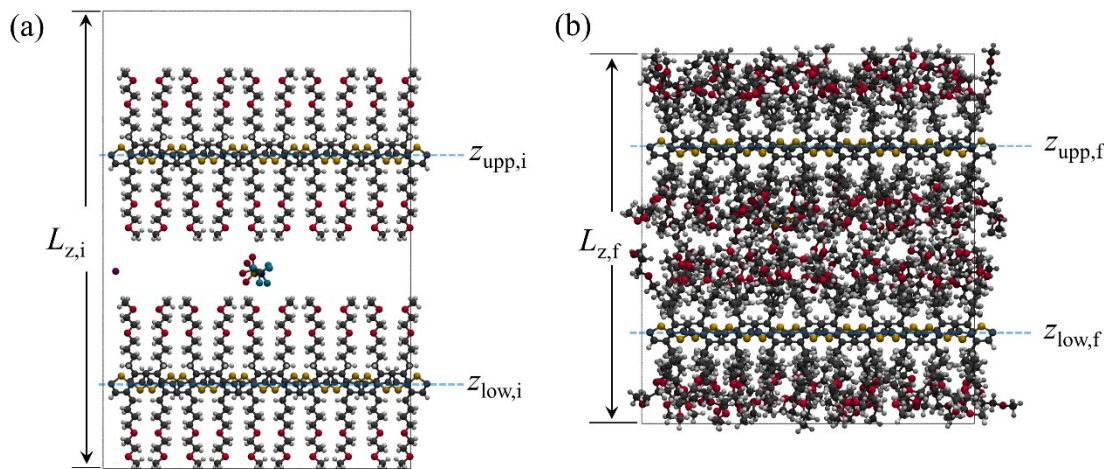


Figure S16 (a) Snapshot of the initial crystalline template with box dimensions: $L_x = 39 \text{ \AA}$, $L_y = 31.2 \text{ \AA}$, $L_{z,i} = 57.94 \text{ \AA}$. $Z_{\text{upp},i}$ and $z_{\text{low},i}$ mark the z-coordinates of the center of mass of two layers of thiophene rings. (b) Snapshot of the final equilibrated crystalline morphology with the box dimensions: $L_x = 39 \text{ \AA}$, $L_y = 31.2 \text{ \AA}$, $L_{z,f} = 43.206 \text{ \AA}$. $Z_{\text{upp},f}$ and $z_{\text{low},f}$ mark the z-coordinates of the center of mass of two layers of thiophene rings. With the LiTFSI salt added in the middle of the simulation box, the distance between two thiophene layers can be slightly larger than the half of the box length, i.e., $Z_{\text{upp},f} - z_{\text{low},f} \geq 0.5L_{z,f}$.

Figure S17 shows the LAMMPS command template we used to generate the equilibrated crystalline morphology. The whole system is divided into three groups, including thiophene rings in the upper layer, thiophene rings in the lower layer and all side chains. During the equilibration, all side chains are allowed to move freely. Meanwhile, the two layers of thiophene rings move with a constant speed in the z-axis, $\mathbf{v} = (0, 0, v_z)$, so that the relative position of thiophene atoms remains the same as that in the polymorph I of P3HT. The constant speed for each layer of thiophenes is usually different, and is calculated by:

$$v_{z,\text{upp}} = \frac{Z_{\text{upp},f} - Z_{\text{upp},i}}{\Delta t}, v_{z,\text{low}} = \frac{z_{\text{low},f} - z_{\text{low},i}}{\Delta t} \text{ Equation S5}$$

where Δt is the total time of this equilibration process. Before the calculation of PMF, the configuration shown in Figure S16(b) is further equilibrated in a number, volume, temperature (NVT) canonical ensemble simulation for some extra time with thiophenes being frozen. It is noted

that sometimes it is necessary to remove some hydrogen atoms of the thiophene at the chain end to avoid an unphysical geometry. Since the thiophene backbone in the crystalline morphology only serves as anchors for side chains, this slight modification is inconsequential (see Figure S18).

```
# dividing the system into 3 groups
group sidechain [option]
group lowThiophene [option]
group upThiophene [option]

# initializing the velocity of each group
velocity sidechain create [targeted temperature option] mom yes rot yes dist gaussian
velocity lowThiophene set 0 0 [  $v_{z,low}$  ] sum no units box
velocity upThiophene set 0 0 [  $v_{z,upp}$  ] sum no units box

# deforming the box, equilibrating side chains
fix 1 liquid deform 1 z final -20.171 20.171 units box remap v
fix 2 liquid nvt/sllod temp [targeted temperature option]
# zeroing the force on the thiophene rings to generate constant speed motion
fix 3 upThiophene setforce 0.0 0.0 0.0
fix 4 upThiophene nve
fix 5 lowThiophene setforce 0.0 0.0 0.0
fix 6 lowThiophene nve
```

Figure S17 LAMMPS template used in this work to generate the equilibrated crystalline morphology. The text in the square brackets can be filled with certain options provided by LAMMPS. To make full use of this template, the reader should visit the LAMMPS website for detailed explanation and writing suggestion.

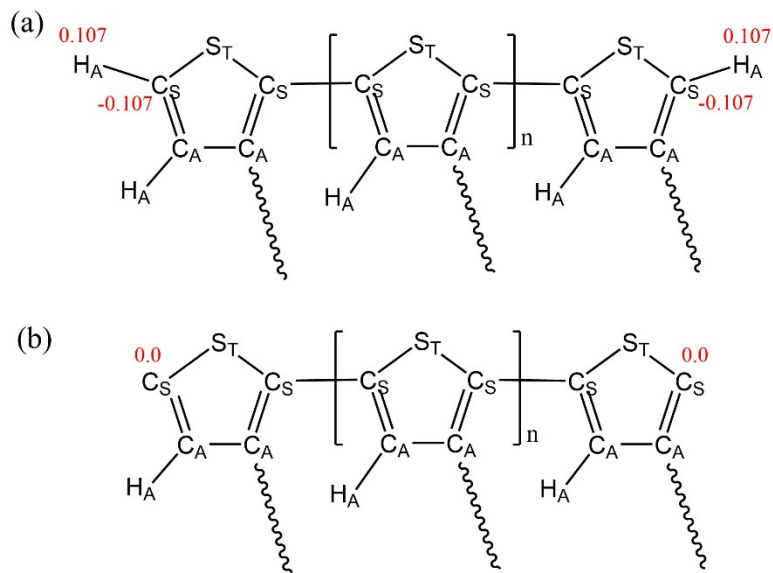


Figure S18 (a) The chemical structure of the full polythiophene backbone. (b) The chemical structure of the slightly modified polythiophene backbone to fit into the crystalline morphology. Atoms of different types in our atomistic model are labeled with different letter subscripts. The red number indicate the partial charge of a certain atom.

S.6.2.2 Amorphous Morphology

Generation of the amorphous morphology is relatively straightforward. The initial configuration can be a crystalline template as described in the last section, or any customized random configuration generated by other software. Then we can increase the temperature of the system to a higher value (e.g., 600 K) to allow the system to fully disorder (*i.e.*, effectively melting the crystals). Finally, the system is rapidly quenched back to room temperature or to another target simulation temperature to lock in the predominantly amorphous morphology.

Here, we provide an alternative approach used in this work to generate the amorphous morphology for the reader's reference. Figure S19a shows the initial configuration, where the crystalline template is arranged in a cubic box ($L_x = L_y = L_z = 52$ Å). There are 16 polymer chains in the system, and each chain contains 10 repeat units. An number, pressure, temperature (*NPT*) ensemble is employed at 101 kPa and the target simulation temperature (*e.g.*, 400 K). Meanwhile, we change the interaction strength of the pair potentials (*i.e.*, Lennard-Jones and Coulombic potential) to the ratio of 0.1 of the full strength, and then gradually increase them back to full

strength set by force field parameters. This operation can be done by the “adapt” command in the LAMMPS. Before any dissociation calculations, the generated amorphous configuration (see Figure S19b) is further equilibrated in a NVT ensemble with a pre-defined box dimension ($L_x = L_y = L_z = 37.56 \text{ \AA}$). The justification for adopting a universal box length across different species is similar to that presented in the section of crystalline morphology.

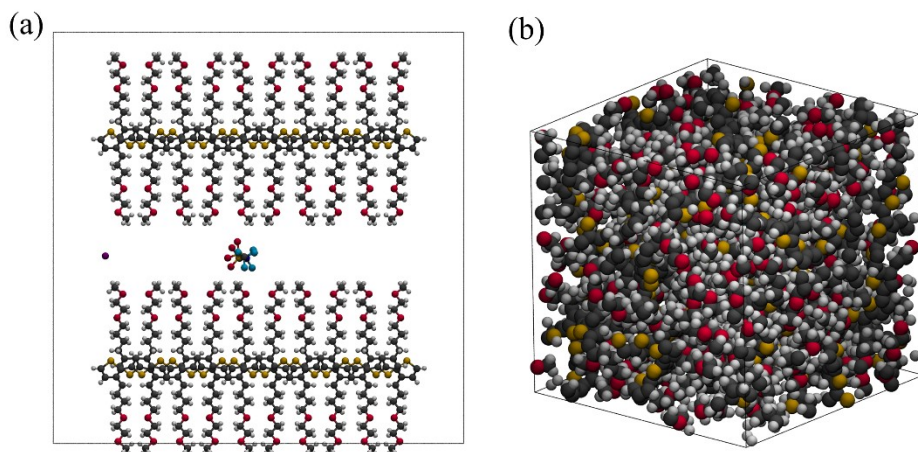


Figure S19 (a) Snapshot of the initial crystalline template with the box dimensions: $L_x = L_y = L_z = 52 \text{ \AA}$. (b) Snapshot of the final equilibrated amorphous morphology with the box dimensions: $L_x = L_y = L_z = 37.56 \text{ \AA}$.

S.6.3 Lithium Ion Mobility Calculations

To simulate the mobility of ions in each polymer, Li^+ ions were introduced at a salt-to-repeat-unit ratio of $r = 0.15$ into each of the equilibrated structures, *e.g.*, 24 Li^+ ions were randomly added into the 160-repeat-unit system discussed in Section S.6.2. A unidirectional electric field of 0.5 V/nm was applied along the x -axis (following the same coordinate system adopted in Section S.6.2). Simulations were run for 20 ns in a *NVT* ensemble at the temperature of 400 K to allow for better sampling.

Under the electric field, the motion of ions and polymers is tracked by simulation trajectories, and any drift motion of the whole system is also tracked. To study the ion transport relative to the surrounding polymers, we need to separate the drift motion of polymers and the migration of ions.

For every simulation trajectory, the center of mass (COM) of all polymers in each frame is calculated, and then a new ion trajectory is generated by subtracting this COM from the original coordinates of ions. This new ion trajectory is used to calculate the MSD. Due to the intermittent hopping events during the individual ion transport process, the average of these individual ion MSDs is calculated to obtain a smooth graph.

At long times, the average ion motion is expected to yield a linear response behavior (Ohm's law) under the external electric field, giving a curved MSD vs time interval (Δt) plot (see Figure S20a). The ion mobility is extracted following the relation in Equation S6, where v is the average drift velocity of ions relative to the moving polymer frame. This relative drift velocity is a product of the applied electric field, E , and the ion mobility, μ . Note that there is usually a developing regime in the short-time-interval period before the MSD plot reaches to the linear-response regime in the long-time-interval period. The length of the developing regime depends on the polymer species. In the plot of MSD vs Δt^2 (see Figure S20b), we found that the time-interval period of $\Delta t > 5$ ns ($\Delta t^2 > 25$ ns²) is relatively long enough for ions to reach linear-response regime. Therefore, the relative drift velocity of Li⁺ ions is extracted from the slope of the MSD vs Δt^2 plot in the time-interval period of $\Delta t > 5$ ns ($\Delta t^2 > 25$ ns²) through linear regression.

$$MSD \sim (vt)^2 = (E\mu)^2 t^2 \quad \text{Equation S6}$$

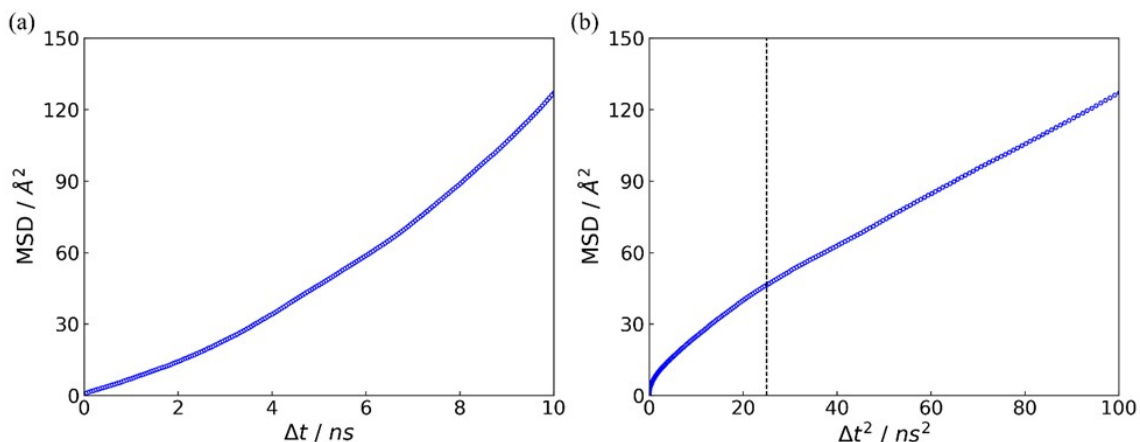


Figure S20: Average mean-squared displacements of ions in the crystalline phase of P3AAPT. (a) MSD vs Δt . (b) MSD vs Δt^2 .

S.6.4 Dissociation Energy and Potential of Mean Force

Variations in the concentration of oxygen containing groups was monitored to assess the effect on dissociation of lithium salts. To model the dissolution of salts, we can use an Arrhenius expression which is dependent on the dielectric constant, ϵ , and the activation energy of dissociation, E_a , as well as the Boltzmann constant, k_b , and temperature, T , as shown in Equation S7.⁹

$$\text{rate} \propto e^{\frac{-E_a}{\epsilon k_b T}} \quad \text{Equation S7}$$

The same salt pairing will have the same E_a across all polymers; the varying component will be ϵ . As such, we can create a modified energy term, E_d , which represents the ratio of E_a and ϵ , and insert it into a more standard conductivity equation to define a polymer-specific environment for ion-dissolution processes.

For any given polymer, E_d is approximated by the free energy barrier for dissociation of a salt pair (LiTFSI) in the polymer medium. For an isotropic environment, such as bulk water, the relative orientation of the salt to the environment is not important due to symmetry; however, for the crystalline and amorphous environments of our systems, there is significant heterogeneity. Therefore, the ion pair is allowed to fully explore rotational degrees of freedom in implementing

umbrella sampling to calculate the potential of mean force (PMF) of LiTFSI dissociation in every proposed polymer chemistry.¹⁰ The reaction coordinate is set to be the separation distance (r_{sep}) between Li^+ and the center of mass (COM) of TFSI. The range of interest of r_{sep} is sampled in a series of windows, which are eventually combined with the weighted histogram analysis method (WHAM).¹¹ In each window, a harmonic bias potential is applied to keep the system close to the reference separation distance r_i^{ref} of the respective window i .

$$\omega_i(r_{\text{sep}}) = \frac{1}{2}K(r_{\text{sep}} - r_i^{\text{ref}})^2 \quad \text{Equation S8}$$

Here, K is chosen to be 16 kcal/(mol·Å²) [1 kcal = 4.814 kJ], and r_i^{ref} is chosen from 3.0 Å to 15.0 Å with an increment of 0.5 Å. In each window, four random initial configurations are used to get better sampling, and each configuration was run for 1 ns to collect the distribution of r_{sep} . Simulations were run at 400 K and employed both the crystalline and amorphous phases of the polythiophene derivatives. For the crystalline morphology, the polythiophene backbone is frozen to keep the lamella configuration. For the amorphous morphology, the polythiophene backbone can move freely without the external constraint. The value of the dissociation energy (E_d) is taken as the difference between the largest and smallest values of the PMF curve. Traces of the observed PMFs for the crystalline and amorphous phases are shown in Figure S21A and B, with the calculated E_d plotted in Figure S21C and summarized in Figure S21D. Poly(3-nonylthiophene) [P3AAAT] was included alongside a purely vacuum dissociation process to highlight the significance of the increased side chain polarity to lower the free energy barrier.

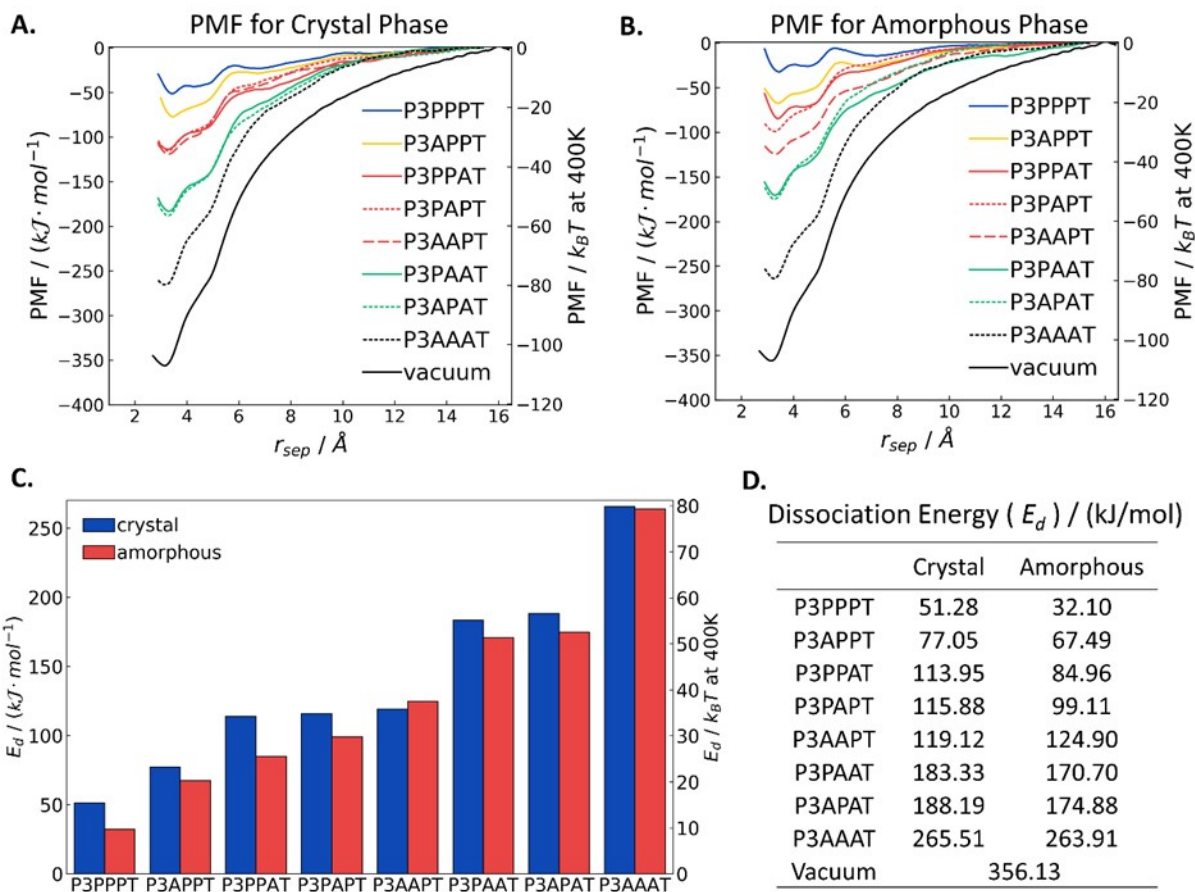


Figure S21: A. Crystalline and, B. Amorphous phase PMF traces for all polymers, including the case of purely alkyl side chains and a full vacuum state for reference. C. Bar plot of calculated E_d in both amorphous and crystalline polymers. D. Values of calculated E_d for all polymers, including the pure alkyl and in vacuum cases for reference.

A summary of all calculated results is shown below, in Tables S5 (crystalline) and S6 (amorphous).

Table S5: Summary of key properties from the simulation of the crystalline phases of all polymers.

Crystalline Phase Simulation Results					
	$v/(\text{\AA}/\text{ns})$	n/nm^{-3}	$E_d/(\text{kJ} \cdot \text{mol}^{-1})$	$\sigma(\text{raw value})$	$\sigma(\text{normalized})$
P3AAPT	1.0333	0.4565	119.1163	0.003960	3.2591
P3APAT	0.1166	0.4565	188.1901	0.000283	0.2328
P3APPT	0.5545	0.4565	77.0535	0.003285	2.7037
P3PAAT	0.3069	0.4565	183.3282	0.000764	0.6289
P3PAPT	1.0265	0.4565	115.8763	0.004044	3.3282
P3PPAT	0.1220	0.4565	113.9465	0.000489	0.4023
P3PPPT	0.1365	0.4565	51.2836	0.001215	1

Table S6: Summary of key properties from the simulation of the amorphous phases of all polymers.

Amorphous Phase Simulation Results					
	$v/(\text{\AA}/ns)$	n/nm^{-3}	$E_d/(kJ \cdot mol^{-1})$	$\sigma(\text{raw value})$	$\sigma(\text{normalized})$
P3-AAP-T	0.3467	0.4529	124.9002	0.001257	0.1527
P3-APA-T	0.1764	0.4529	174.8753	0.000457	0.0555
P3-APP-T	0.4593	0.4529	67.4908	0.003082	0.3745
P3-PAA-T	0.1695	0.4529	170.6951	0.000450	0.0546
P3-PAP-T	0.9525	0.4529	99.1123	0.004353	0.5288
P3-PPA-T	0.4433	0.4529	84.9564	0.002363	0.2871
P3-PPP-T	0.5833	0.4529	32.0965	0.008231	1

S.6.5 Solvation Shells and Solvation Environments

To understand the PMF curves of different polythiophene derivatives, the lithium-ion solvation shell is identified according to the number of coordinating oxygens from the ethylene oxide (EO) unit within the cutoff distance of 4 Å. The Li⁺ ion solvation shell behavior is shown here in Figure S22 for all polymers. As the separation distance increases, the number of coordinating oxygens within the solvation shell also increases, which facilitate the dissociation of LiTFSI. The solvation shell with more coordinating oxygens shows lower dissociation energy. In the crystalline phase, it is postulated that the solvation shell is related to the thickness of EO layers (Figure S23) in the different polythiophene derivatives.

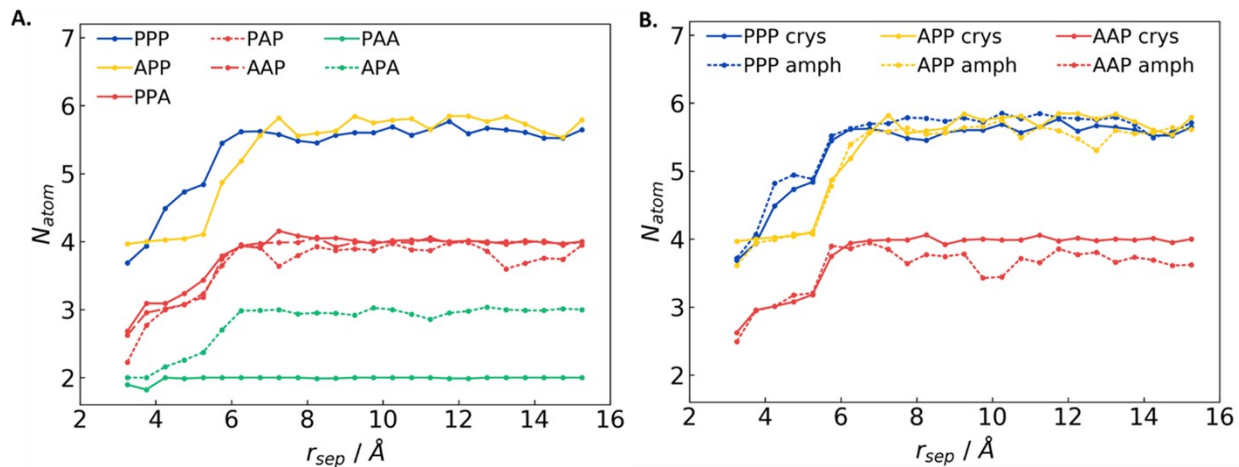


Figure S22: Number of coordinating O from EO groups in Li^+ solvation shell: A. Crystalline polymer, showing similar clustering of curves as was observed for the PMF traces. B. Comparison of crystalline and amorphous solvation shells for a subset of the polymers studied.

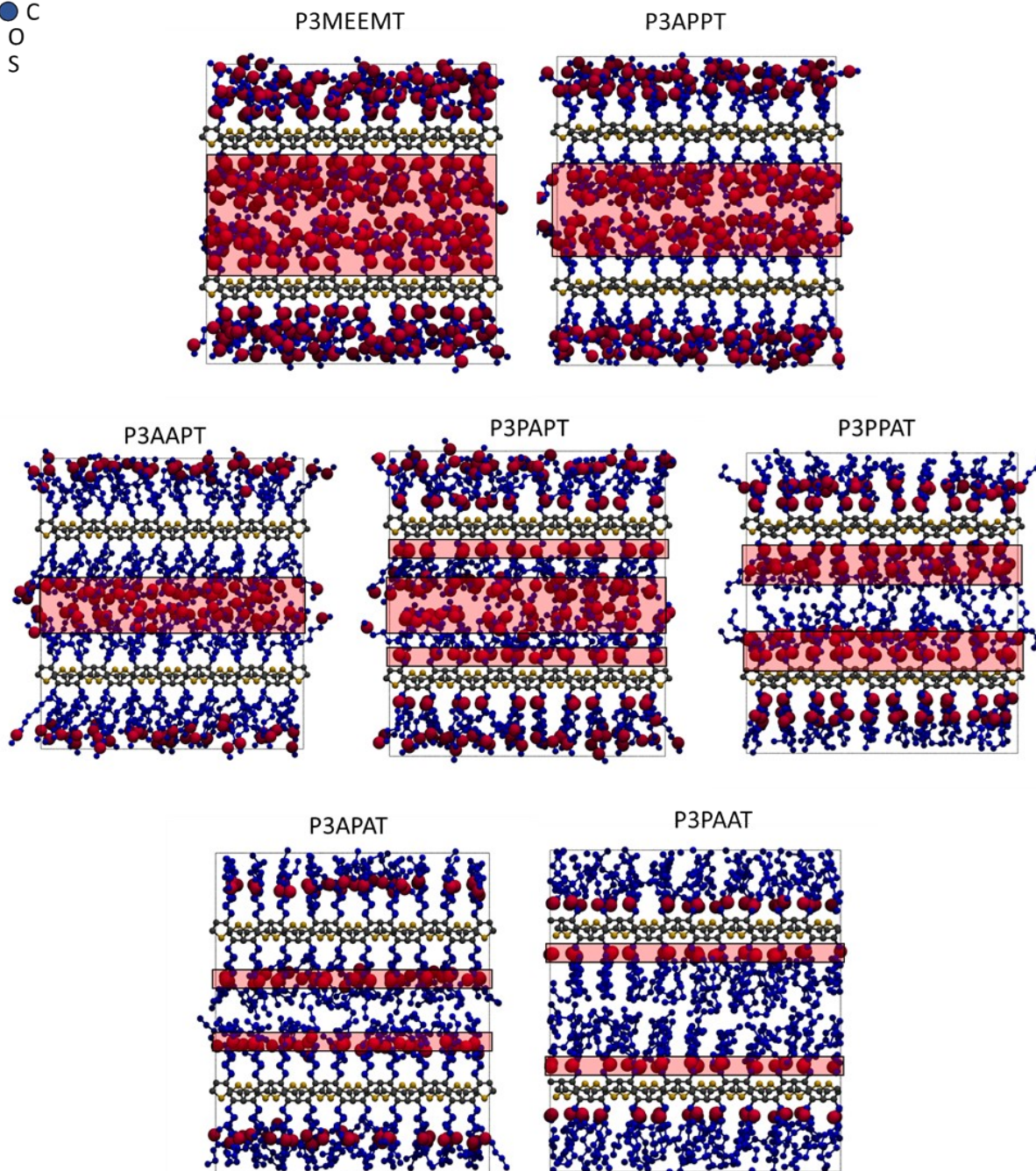


Figure S23: Solvation environments for all polymers *in* crystalline state. The semitransparent red rectangles represent oxygen-rich areas within the side chain domain. The location and approximate thickness of such domains correlate with the relative ease of solubility of Li ions in the different polymers.

S.7. DC measurements for P3AAPT

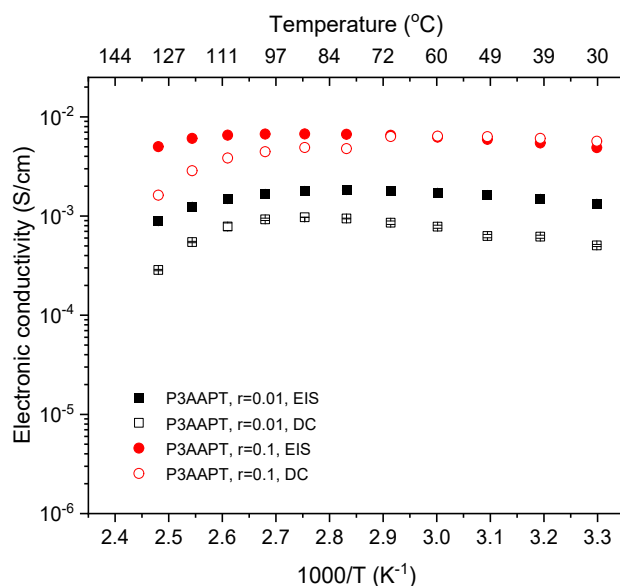


Figure S24: Comparison of electronic conductivities of P3AAPT with different salt concentrations from EIS and DC measurements.

S.8. SI References

- 1 E. Lee, B. Hammer, J.-K. Kim, Z. Page, T. Emrick and R. C. Hayward, *J. Am. Chem. Soc.*, 2011, **133**, 10390–10393.
- 2 B. X. Dong, C. Nowak, J. W. Onorato, J. Strzalka, F. A. Escobedo, C. K. Luscombe, P. F. Nealey and S. N. Patel, *Chem. Mater.*, 2019, **31**, 1418–1429.
- 3 D. M. Huang, R. Faller, K. Do and A. J. Moulé, *J. Chem. Theory Comput.*, 2010, **6**, 526–537.
- 4 W. L. Jorgensen, D. S. Maxwell and J. Tirado-Rives, *J. Am. Chem. Soc.*, 1996, **118**, 11225–11236.
- 5 C. Poelking and D. Andrienko, *Macromolecules*, 2013, **46**, 8941–8956.
- 6 S. Plimpton, *J. Comput. Phys.*, 1995, **117**, 1–19.
- 7 J. N. Canongia Lopes, A. A. H. Pádua and K. Shimizu, *J. Phys. Chem. B*, 2008, **112**, 5039–5046.
- 8 N. Kayunkid, S. Uttiya and M. Brinkmann, *Macromolecules*, 2010, **43**, 4961–4967.
- 9 R. M. Fuoss and C. A. Kraus, *J. Am. Chem. Soc.*, 1933, **55**, 1019–1028.
- 10 J. Kästner, *WIREs Comput. Mol. Sci.*, 2011, **1**, 932–942.
- 11 S. Kumar, J. M. Rosenberg, D. Bouzida, R. H. Swendsen and P. A. Kollman, *J. Comput. Chem.*, 1992, **13**, 1011–1021.

ⁱ Certain commercial equipment, instruments, or materials are identified in this paper in order to specify the experimental procedure adequately. Such identification is not intended to imply recommendation or endorsement by NIST, nor is it intended to imply that the materials or equipment identified are necessarily the best available for the purpose.